

COLOR DISPERSION AS AN INDICATOR OF STELLAR POPULATION COMPLEXITY: INSIGHTS FROM THE PIXEL COLOR-MAGNITUDE DIAGRAMS OF 32 BRIGHT GALAXIES IN ABELL 1139 AND ABELL 2589

JOON HYEOP LEE^{1,2}, MINA PAK^{1,2}, HYE-RAN LEE^{1,2}, SREE OH^{3,4,5}¹ Korea Astronomy and Space Science Institute, Daejeon 34055, Korea² University of Science and Technology, Daejeon 34113, Korea³ Research School of Astronomy and Astrophysics, The Australian National University, Canberra, ACT 2611, Australia⁴ ARC Centre of Excellence for All Sky Astrophysics in 3 Dimensions (ASTRO 3D), Australia⁵ Department of Astronomy and Yonsei University Observatory, Yonsei University, Seoul 03722, Korea*Draft version October 30, 2021*

ABSTRACT

We investigate the properties of bright galaxies with various morphological types in Abell 1139 and Abell 2589, using the pixel color-magnitude diagram (pCMD) analysis technique. The sample is 32 galaxies brighter than $M_r = -21.3$ mag with spectroscopic redshifts, which are deeply imaged in the g and r bands using the MegaCam mounted on the Canada-France-Hawaii Telescope. After masking contaminants with two-step procedures, we examine how the detailed properties in pCMDs depend on galaxy morphology and infrared color. The mean $g - r$ color as a function of surface brightness (μ_r) in the pCMD of a galaxy shows fine performance in distinguishing between early- and late-type galaxies, but it is not perfect because of the similarity between elliptical galaxies and bulge-dominated spiral galaxies. On the other hand, the $g - r$ color dispersion as a function of μ_r works better. We find that the best set of parameters for galaxy classification is the combination of the minimum color dispersion at $\mu_r \leq 21.2$ mag arcsec⁻² and the maximum color dispersion at $20.0 \leq \mu_r \leq 21.0$ mag arcsec⁻²: the latter reflects the complexity of stellar populations at the disk component in a typical spiral galaxy. Finally, the color dispersion measurements of an elliptical galaxy appear to be correlated with the WISE infrared color ([4.6] - [12]). This indicates that the complexity of stellar populations in an elliptical galaxy is related with its recent star formation activities. From this observational evidence, we infer that gas-rich minor mergers or gas interactions may have usually happened during the recent growth of massive elliptical galaxies.

Subject headings: galaxies: clusters: individual (Abell 1139, Abell 2589) — galaxies: elliptical and lenticular, cD — galaxies: spiral — galaxies: evolution — galaxies: formation

1. INTRODUCTION

The comprehensive understanding of the formation histories of galaxies in variety of morphology is a major goal in modern astronomy. Over the classical paradigms about the formation of massive galaxies such as the monolithic collapse model (Patridge & Peebles 1967; Tinsley 1972; Larson 1974) and the hierarchical merging model (Toomre 1977; Searle & Zinn 1978), a huge number of studies in recent decades have illuminated various aspects in the mass assembly and star formation histories of galaxies. Currently, much observational evidence supports a galaxy formation scenario that is more complicated than classically assumed: massive galaxies may have built through two-phase and inside-out formation processes (e.g., van Dokkum et al. 2010; Oser et al. 2010; Lee & Yi 2013; Pastrello et al. 2015; Liu et al. 2016). In this scenario, massive galaxies have experienced violent starburst and subsequent star formation quenching at a relatively early epoch, which partially resembles the classical monolithic collapse. On the other hand, such a violent starburst is thought to be often triggered by gas-rich major mergers as well as those galaxies are found to have kept growing via numerous minor mergers for a long time after the early starburst and quenching, which is consistent with the hierarchical build-up scheme.

Although recent observational and theoretical achieve-

ments shed light on our understanding of galaxy formation by suggesting a reasonable solution to the apparent contradiction between the classical models, however, several detailed issues are still under a veil. For example, it has not been perfectly comprehended how the recent histories of star formation and mass assembly in massive galaxies are related with each other. Several recent studies argued that the major formation process of early-type galaxies depends on their masses, in the context that low-mass early-type galaxies tend to have experienced gas-rich mergers, whereas massive early-type galaxies have grown via dry mergers (Kormendy et al. 2009; Bernardi et al. 2011; Lee et al. 2013). However, whereas those findings well explain the average trends of galaxy formation, we witness various exceptions such as massive galaxies with evidence of recent star formation activities (e.g., Lee et al. 2006; Fernández-Ontiveros et al. 2011; George 2017; Sheen et al. 2017).

It is relatively easy to trace current or recent star formation in a galaxy by using various well-defined indicators, such as optical or UV - optical colors, spectral emission lines, and infrared or radio luminosity. On the other hand, the method to trace recent mass assembly events is not very well established, compared to star formation measurement. One may determine whether a galaxy recently experienced merging events or not, by decomposing its internal structures and estimating its structural asymmetry or irregularity. However, such an

approach requires much effort for each galaxy, as well as quantitative comparison between different galaxies is not easy. Thus, if a simple and efficient indicator of recent mass assembly is devised, it will be very useful for investigating recent evolution histories of a large number of galaxies, in combination with the tracers of recent star formation activities.

A candidate for such a simple and efficient methodology to trace the formation history of a galaxy is the pixel color-magnitude diagram (pCMD) analysis (Bothun 1986; Abraham et al. 1999; de Grijs et al. 2003; Lanyon-Foster et al. 2007; Lee et al. 2011, 2012, 2017). This method has not been very widely used until now, but it has potential to be a powerful approach to total understanding of the photometric and structural properties of galaxies. For example, Lanyon-Foster et al. (2007) showed that galaxies in variety of morphological types show various and distinct features in their pCMDs, such as *prime sequences* for early-type galaxies and *inverse-L* features for spiral galaxies. Compared to the classical photometric and/or structural analysis methods, the pCMD analysis has several advantages: (1) it can be consistently applied to galaxies with any kind of morphology, (2) it considers the photometric and structural properties at the same time, and (3) it is efficient in checking the homology between galaxies in different mass or size scales (Lee et al. 2017).

Despite such merits, however, the usage of the pCMD analysis is not perfectly established yet. As an effort to devise a quantitative analysis method using pCMDs, Lee et al. (2017) introduced simple routines to compare pCMDs to check the similarity in galaxy formation history. They compared the brightest cluster galaxies (BCGs) in Abell 1139 (A1139) and Abell 2589 (A2589) using the pCMD analysis technique, which are two of the 14 galaxy clusters targeted in the KASI-Yonsei Deep Imaging Survey of Clusters (KYDISC; Oh et al. 2018). By simplifying the overall pCMD features into the mean and standard deviation of pixel color as a function of pixel surface brightness (called a pCMD *backbone*), Lee et al. (2017) showed that the BCG of dynamically relaxed A2589 formed a larger central body at an early epoch and has grown to be a larger, more massive and dynamically better relaxed galaxy today than the BCG of dynamically young A1139. Those results support the idea that a BCG and its host cluster coevolve.

As shown in Lee et al. (2017), the pCMD backbone analysis is a useful method for comparing the formation histories of galaxies even with different mass or size scales, but it needs to be more simplified to be efficiently applied to a large number of galaxies. One of the remarkable quantities is the color dispersion at given μ_r in a pCMD. This quantity is thought to reflect the complexity of stellar populations. That is, a dynamically young galaxy, in which multiple stellar populations are not well mixed spatially, must have large color dispersion. Based on this inference, Lee et al. (2017) concluded that the BCG of A1139 is dynamically younger than the BCG of A2589. However, since BCGs usually have simple structures, it will be worth examining the performance of this parameter for more various galaxies.

This is the second of the series papers presenting the pCMD analysis results of the KYDISC cluster galaxies. In this paper, we present our pCMD study of 32 bright

galaxies in A1139 and A2589. The goals of this paper are (1) to examine how the pCMD properties depend on galaxy morphology quantitatively, and (2) to understand how the stellar population complexity of a galaxy indicated by color dispersion in a pCMD is related with recent star formation activity represented by infrared color. This paper is outlined as follows. Section 2 describes observations and sample selection. Section 3 presents the standard and alternative procedures for masking contaminants to yield final pCMDs. The results about the pCMD properties depending on morphology and star formation activity are shown in Section 4. The implication of our results is discussed in Section 5, and finally the conclusions are drawn in Section 6. In Appendix, additional figures showing the detailed processes of masking contaminants are presented, and the final results after the alternative masking procedure are shown, which are in good agreement with the results after the standard masking procedure. Throughout this paper, we adopt the cosmological parameters: $h = 0.7$, $\Omega_\Lambda = 0.7$, and $\Omega_M = 0.3$.

2. OBSERVATIONS AND TARGETS

2.1. CFHT Observations and Sample Selection

Our data set were obtained using the MegaCam mounted on the 3.6-meter Canada-France-Hawaii Telescope (CFHT) in 2012 – 2013, as a part of the KYDISC project. Among the 14 nearby clusters at $0.016 \leq z \leq 0.145$ observed in the KYDISC project, the target clusters in this paper are A1139 and A2589, which are at very similarly low redshifts ($z \sim 0.04$). This similarity in redshift makes the pCMD comparison much easier, because the galaxies in the two target clusters have almost the same conversion factors from angular size to physical scale (~ 0.8 kpc per arcsec) and central wavelengths at the rest frame. See Table 1 of Lee et al. (2017) for the basic information of the two target clusters.

In the g and r bands respectively, each cluster was deeply imaged with total exposure time of 2940 seconds. After pre-processing and image stacking, the finally re-sampled pixel scale is $0.185''$ and the stellar full width at half maximum (FWHM) is about $0.8''$. Based on the redshift information retrieved from the Sloan Digital Sky Survey (York et al. 2000), NASA Extragalactic Database¹ and SIMBAD Astronomical Database², cluster members were selected by using the difference in recession velocity from the host cluster ($|\Delta v_{rec}| \leq 3\sigma_{cl}$) and the clustercentric distance ($R \leq 2R_{200}$), where σ_{cl} and R_{200} are the velocity dispersion and virial radius of a given cluster, respectively. More details about the KYDISC project and its data products are described in Oh et al. (2018).

In this paper, we investigate the bright ($M_r \leq -21.3$ mag) galaxies in A1139 and A2589 using the pCMD analysis method. Among the selected cluster members, there are 16 and 15 galaxies brighter than the magnitude cut in A1139 and A2589, respectively. In addition to these 31 member galaxies, there is a bright galaxy (A1139-00004) that satisfies $|\Delta v_{rec}| \leq 3\sigma_{cl}$ but is located at $2.2 \times R_{200}$ distance from the A1139 center. This galaxy is not a

¹ <http://ned.ipac.caltech.edu>

² <http://simbad.u-strasbg.fr/simbad/>

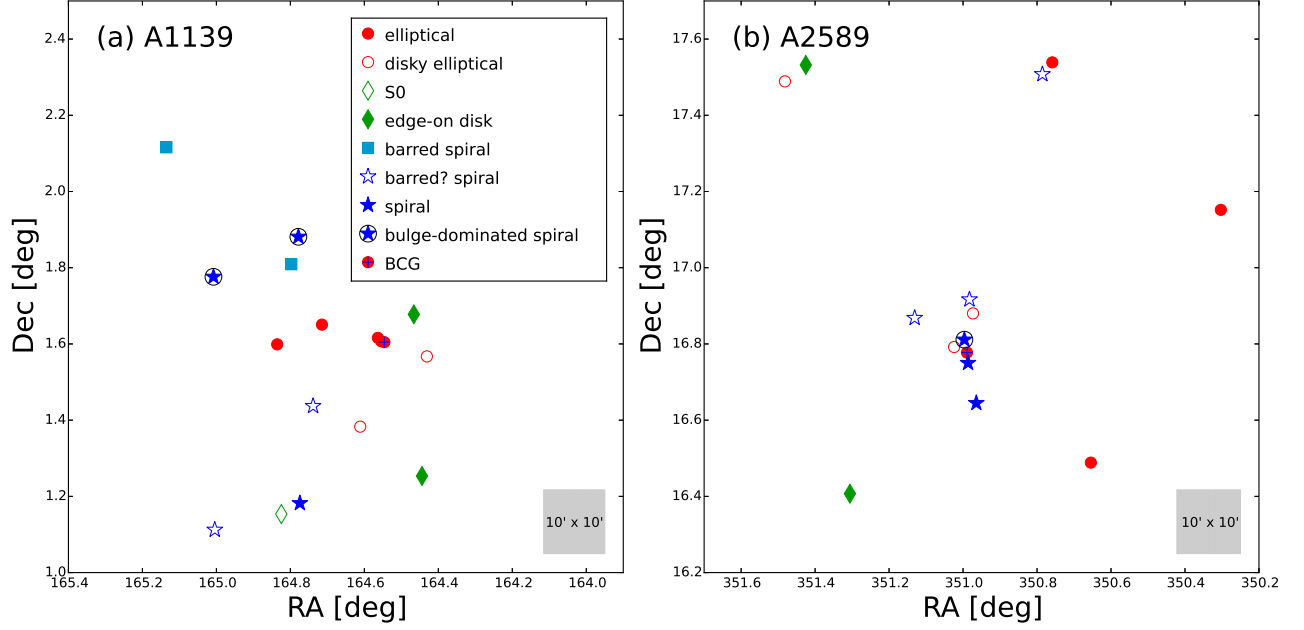


FIG. 1.— Spatial distribution of the sample galaxies in (a) A1139 and (b) A2589. The visually classified morphological types are denoted (see Section 2.2 for the details). The gray box in each panel shows the angular scale of 10×10 square arcminutes ($\approx 0.5 \times 0.5$ Mpc 2).

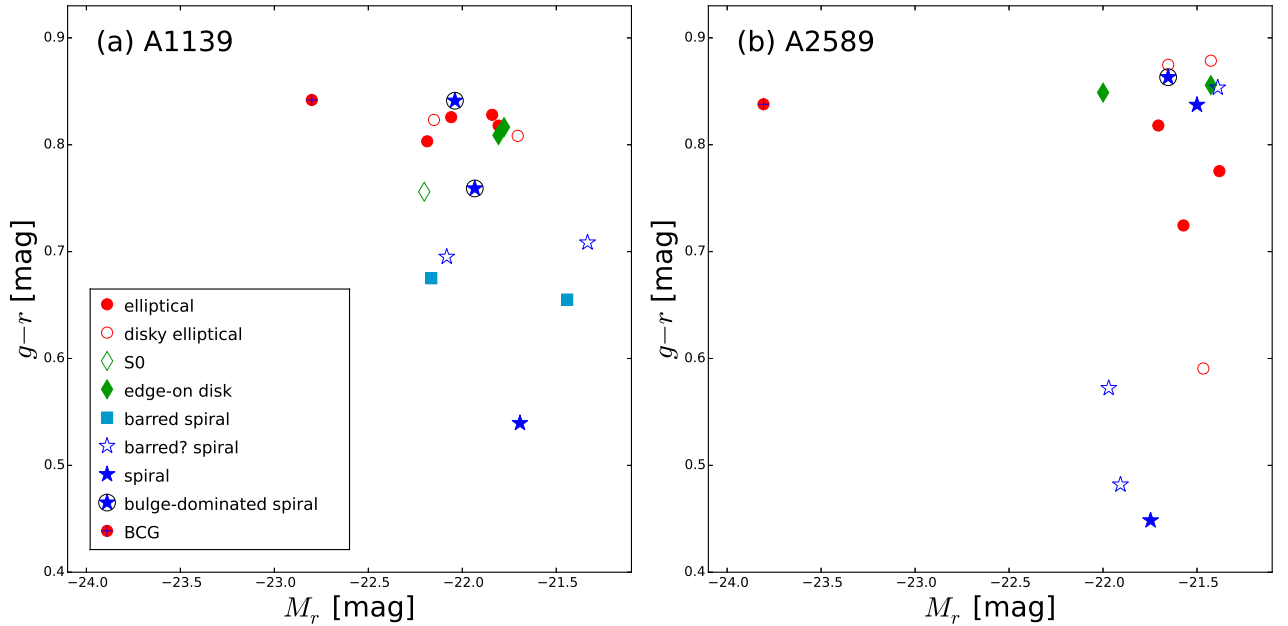


FIG. 2.— Total color-magnitude diagrams of the sample galaxies in (a) A1139 and (b) A2589, with the morphological types denoted.

member of A1139 in our selection criteria, but we include this galaxy in our sample, too. Since this paper is not focused on environmental effects, the important is the fact that this galaxy is at a distance from us similar to those of the cluster members, not its membership itself.

In this paper, we apply k -correction to neither pixel surface brightness nor total magnitude, because the k -correction based on 2-band color may not be sufficiently reliable, particularly when the photometric uncertainty is large (e.g., faint pixels). On the other hand, Lee et al. (2017) did not apply k -correction to pixel surface bright-

ness either, but they applied it to total magnitude when selecting cluster members for comparison with BCGs. Thus, the sample in this paper does not exactly coincide with the comparison sample in Lee et al. (2017). Despite such difference from Lee et al. (2017), we decided that the photometric consistency between the pixel and total magnitudes is more important in this paper.

The basic information of our sample galaxies is summarized in Table 1. The right ascensions (RAs) and declinations (Decs) are for the J2000 epoch. All magnitudes and surface brightness in this paper were corrected for the Galactic extinction using the method of Schlafly &

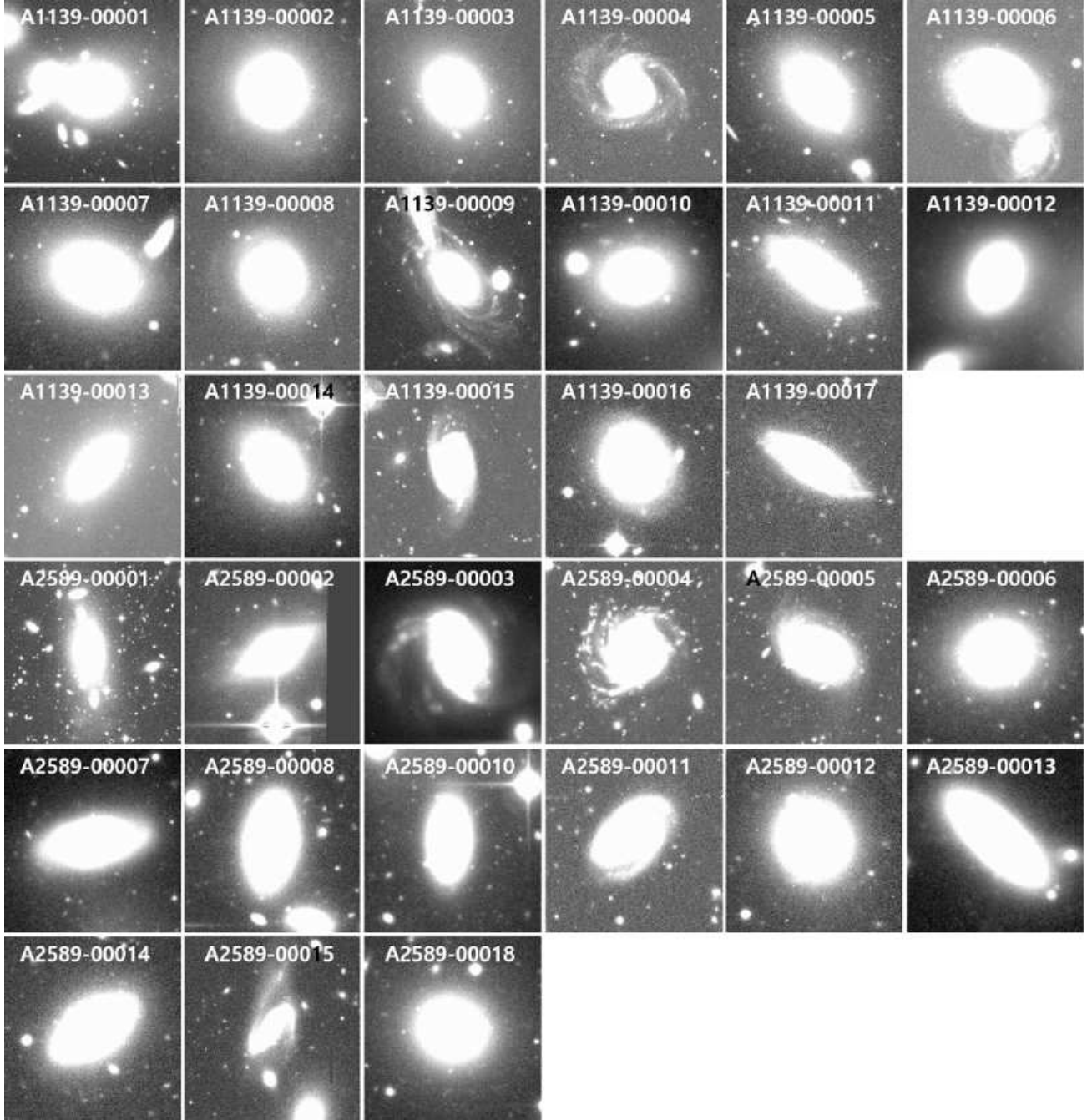


FIG. 3.— Portrait images of the sample galaxies in the r band. The name denoted at the upper side in each panel is the identity number in the KYDISC catalog.

Finkbeiner (2011), in the AB magnitude system. Figure 1 presents the spatial distribution of the selected sample galaxies, while their total color-magnitude diagrams are shown in Figure 2. The r -band portrait images of our sample galaxies are displayed in Figure 3.

2.2. Morphological Classification

Figure 4 shows the r -band surface brightness (μ_r) maps, which reveal the internal structures of our sample galaxies more clearly. Based on Figures 3 and 4, JHL, MP and HRL visually classified the morphological types of our sample galaxies into the following classes:

- Typical elliptical (E): well-defined elliptical struc-

tures without any disturbed features,

- Disky elliptical (disky E): overall elliptical morphology with slightly disk-like internal structures (but not significantly different from typical elliptical galaxies),
- Lenticular (S0): hosting a faint disk component and not significantly inclined (face-on),
- Edge-on disk: largely inclined S0 or late-type (but mostly bulge-dominated in our sample),
- Barred spiral: spiral arms connected to a bar structure (a question mark is denoted when the bar is

TABLE 1
BASIC INFORMATION OF THE SAMPLE GALAXIES

| Name | RA [hh:mm:ss] | Dec [dd:mm:ss] | Redshift | M_r [mag] | $g - r$ [mag] | $ \Delta v_{rec} /\sigma_{cl}$ | R/R_{200} | B/T | Morphology |
|-------------|------------------|-------------------|----------|----------------|------------------|--------------------------------|-------------|------|--------------------------|
| A1139-00001 | 10:58:11.0 | +01:36:17 | 0.038 | -22.801 | 0.842 | 0.88 | 0.27 | 0.94 | elliptical (BCG) |
| A1139-00002 | 10:59:17.9 | +01:09:12 | 0.039 | -22.202 | 0.756 | 0.21 | 1.15 | 0.61 | S0 |
| A1139-00003 | 10:58:51.5 | +01:39:02 | 0.040 | -22.187 | 0.803 | 0.04 | 0.62 | 0.82 | elliptical |
| A1139-00004 | 11:00:32.4 | +02:06:57 | 0.039 | -22.165 | 0.675 | 0.26 | 2.17 | 0.21 | barred spiral |
| A1139-00005 | 10:58:26.7 | +01:22:59 | 0.041 | -22.151 | 0.823 | 0.69 | 0.37 | 0.70 | disky elliptical |
| A1139-00006 | 10:58:57.2 | +01:26:13 | 0.041 | -22.083 | 0.695 | 1.12 | 0.57 | 0.26 | barred? spiral |
| A1139-00007 | 10:59:20.5 | +01:35:56 | 0.039 | -22.059 | 0.826 | 0.48 | 0.83 | 0.69 | elliptical |
| A1139-00008 | 11:00:01.9 | +01:46:34 | 0.040 | -22.039 | 0.841 | 0.30 | 1.40 | 0.42 | spiral (bulge-dominated) |
| A1139-00009 | 10:59:06.8 | +01:52:52 | 0.041 | -21.934 | 0.759 | 0.56 | 1.15 | 0.65 | spiral (bulge-dominated) |
| A1139-00010 | 10:58:15.2 | +01:36:58 | 0.039 | -21.841 | 0.828 | 0.32 | 0.31 | 0.58 | elliptical |
| A1139-00011 | 10:57:51.9 | +01:40:40 | 0.041 | -21.808 | 0.809 | 1.04 | 0.46 | 0.44 | edge-on disk |
| A1139-00012 | 10:58:13.0 | +01:36:25 | 0.039 | -21.807 | 0.818 | 0.85 | 0.28 | 0.64 | elliptical |
| A1139-00013 | 10:57:46.6 | +01:15:13 | 0.039 | -21.778 | 0.817 | 0.41 | 0.64 | 0.87 | edge-on disk |
| A1139-00014 | 10:57:43.4 | +01:34:02 | 0.039 | -21.705 | 0.808 | 0.41 | 0.28 | 0.77 | disky elliptical |
| A1139-00015 | 10:59:05.8 | +01:10:55 | 0.039 | -21.693 | 0.540 | 0.57 | 1.02 | 0.03 | spiral |
| A1139-00016 | 10:59:11.4 | +01:48:33 | 0.040 | -21.442 | 0.655 | 0.10 | 1.04 | 0.44 | barred spiral |
| A1139-00017 | 11:00:01.1 | +01:06:44 | 0.039 | -21.334 | 0.709 | 0.59 | 1.55 | 0.09 | barred? spiral |
| A2589-00001 | 23:23:57.5 | +16:46:38 | 0.041 | -23.807 | 0.838 | 0.09 | 0.04 | 0.98 | elliptical (BCG) |
| A2589-00002 | 23:25:42.0 | +17:31:55 | 0.041 | -22.000 | 0.849 | 0.06 | 1.04 | 0.44 | edge-on disk |
| A2589-00003 | 23:23:08.5 | +17:30:28 | 0.038 | -21.970 | 0.572 | 1.12 | 0.89 | 0.17 | barred? spiral |
| A2589-00004 | 23:24:31.4 | +16:52:05 | 0.036 | -21.907 | 0.482 | 1.89 | 0.20 | 0.39 | barred? spiral |
| A2589-00005 | 23:23:51.4 | +16:38:41 | 0.035 | -21.747 | 0.448 | 2.20 | 0.20 | 0.09 | spiral |
| A2589-00006 | 23:22:37.1 | +16:29:19 | 0.037 | -21.706 | 0.818 | 1.36 | 0.55 | 0.72 | elliptical |
| A2589-00007 | 23:23:59.1 | +16:48:40 | 0.043 | -21.654 | 0.863 | 0.39 | 0.03 | 0.91 | spiral (bulge-dominated) |
| A2589-00008 | 23:23:53.5 | +16:52:48 | 0.045 | -21.653 | 0.875 | 1.17 | 0.09 | 0.30 | disky elliptical |
| A2589-00010 | 23:23:56.8 | +16:44:60 | 0.038 | -21.500 | 0.837 | 1.01 | 0.07 | 0.68 | elliptical |
| A2589-00011 | 23:25:55.6 | +17:29:21 | 0.046 | -21.466 | 0.591 | 1.55 | 1.03 | 0.03 | spiral |
| A2589-00012 | 23:25:13.4 | +16:24:26 | 0.039 | -21.427 | 0.856 | 0.78 | 0.63 | 0.40 | disky elliptical |
| A2589-00013 | 23:24:05.8 | +16:47:31 | 0.042 | -21.426 | 0.879 | 0.09 | 0.06 | 0.73 | edge-on disk |
| A2589-00014 | 23:23:55.8 | +16:55:00 | 0.041 | -21.390 | 0.853 | 0.06 | 0.13 | 0.62 | disky elliptical |
| A2589-00015 | 23:23:02.1 | +17:32:20 | 0.038 | -21.381 | 0.775 | 1.24 | 0.93 | 0.69 | barred? spiral |
| A2589-00018 | 23:23:54.4 | +16:40:50 | 0.045 | -21.321 | 0.828 | 1.24 | 0.16 | 0.68 | elliptical |

ambiguous), and

- Spiral: spiral arms without a bar structure.

Since the bulge fraction affects the overall properties of a late-type galaxy, a mark of ‘BD’ is additionally noted for a bulge-dominated late-type galaxy. The morphological classification is sometimes ambiguous: E versus disky E; disky E versus S0; and S0 versus bulge-dominated spiral. However, the small ambiguity between some types does not significantly matter in this paper, because this paper is mainly focused on the difference between broadly divided early- and late-type galaxies rather than between individual fine classes. Note that the classification in this paper was conducted independently of that in the KYDISC catalog, and thus they may not necessarily coincide with each other. For example, A1139-00008 is listed as an S0 galaxy in the KYDISC catalog, but we classify it into a bulge-dominated spiral, because of very faint ambient features around it. As a quantitative indicator of morphology, we also estimated the bulge-to-total ratio (B/T) of each galaxy, based on the decomposition into Sersic component (bulge) + exponential component (disk) using the GALFIT code (Peng et al. 2002, 2010).

Figure 5 presents the $g - r$ color maps of our sample galaxies. The internal distributions of stellar populations are revealed in these maps, which are particularly useful to visually inspect the interactions with neighbor galaxies (e.g., A1139-00009 and A1139-00017). Note that our morphological classification is not based on these color maps, but only based on the light distributions in the r band.

2.3. WISE Data

Infrared color is a useful tool to diagnose star formation and galactic nuclei activities of galaxies (Assef et al. 2010; Jarett et al. 2011, 2017; Ko et al. 2016). In this paper, we use the Wide-field Infrared Survey Explorer (WISE; Wright et al. 2010) data. The WISE mapped the whole sky in four infrared bands: 3.4, 4.6, 12 and 22 μm (W1, W2, W3 and W4) with angular resolutions of 6.1'', 6.4'', 6.5'', and 12.0'', respectively.

From the WISE website³, we retrieved infrared magnitudes for our target galaxies. For most point-like sources in the WISE data, the recommended magnitude type is the *profile-fit magnitude*, but we use the *elliptical aperture magnitude* instead, because our targets are mostly extended sources even in the WISE images. The elliptical apertures in the WISE photometry are based on the cross-matching with the Two Micron All Sky Survey Extended Source Catalog (2MASS XSC; Skrutskie et al. 2006). However, the aperture magnitude is not available for one of our targets (A2589-00014), which means that this object looks like a point source in the infrared images although it is an extended source in higher resolution. Thus, we use the profile-fit magnitudes only for A2589-00014.

We adopt the [4.6] – [12] (W2 – W3) color as a star formation indicator, because the [12] band flux is sensitive to star formation activity whereas the [4.6] band flux reflects age-independent stellar mass. On the other hand, the [3.4] – [4.6] (W1 – W2) color is known to be

³ <http://wise2.ipac.caltech.edu/docs/release/allsky/>

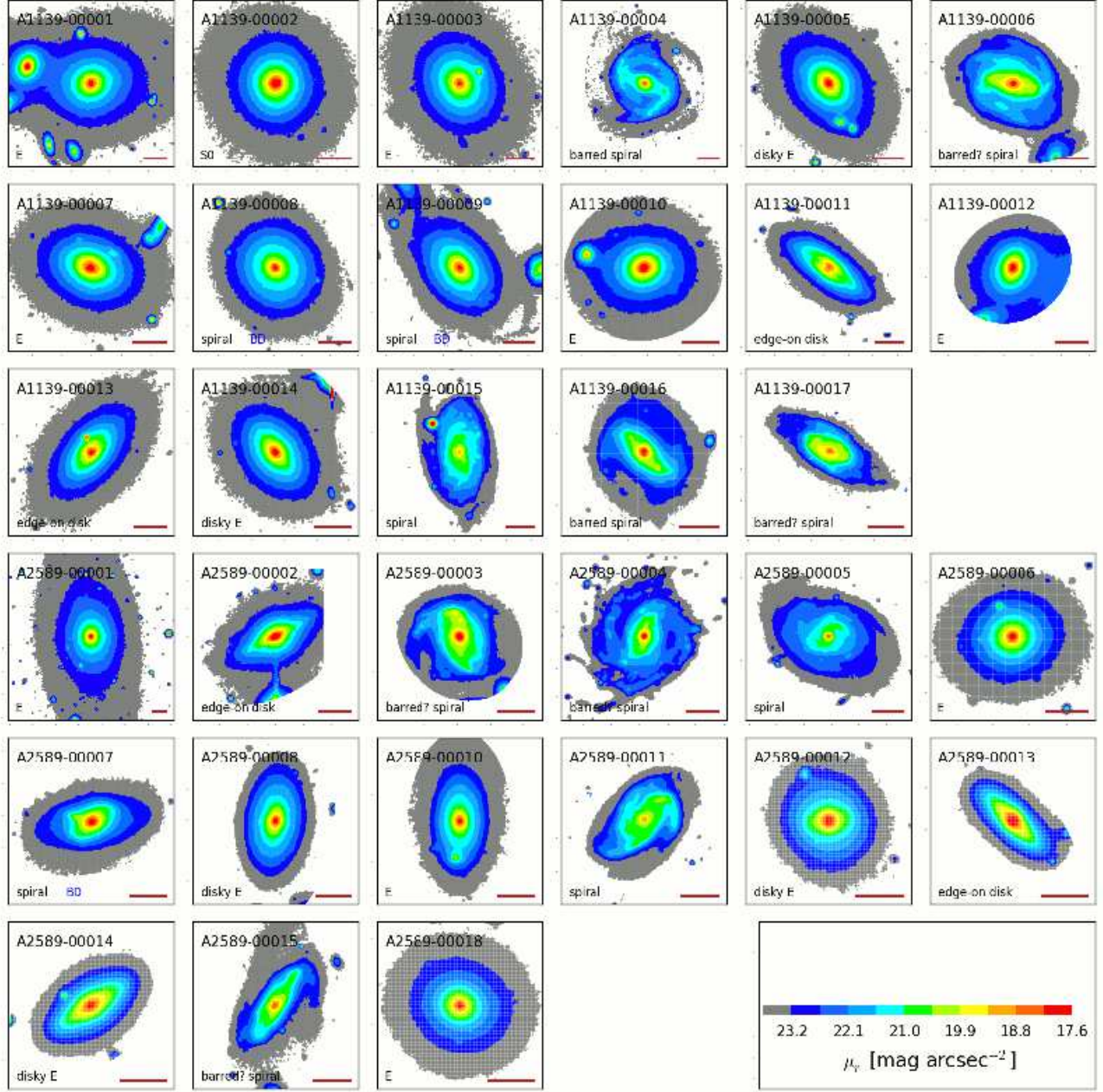


FIG. 4.— The r -band surface brightness maps of the sample galaxies. Visually classified morphology is denoted at the lower left corner and the 10 arcsec (~ 8 kpc) scale bar is shown at the lower right corner in each panel. See the main text for the detailed description of each morphological type.

an indicator of active galactic nuclei (AGNs), owing to its sensitivity to hot dust (Jarett et al. 2017). These color indices are used to describe the star formation properties of the sample galaxies.

3. ANALYSIS

3.1. Standard Procedure for Masking Contaminants

Before plotting final pCMDs, target images need to be appropriately processed, to minimize the influence of contaminants and to improve the signal-to-noise ratio of each pixel. Lee et al. (2017) established a procedure for the pCMD analysis, which includes contaminants-masking and pixel-smoothing. The procedure is summarized as follows:

1. Trim a sufficient area around a target galaxy,
2. Detect objects using the Source Extractor (SE; Bertin & Arnouts 1996) with sufficiently large background mesh sizes (to detect relatively large contaminants),
3. Use the SE again with small background mesh sizes (to detect small and faint contaminants)
4. Mask the pixels within the apertures of any detected non-target objects, and
5. Smooth pixels by adopting a smoothing kernel with a seeing-sized ($0.8''$) aperture.

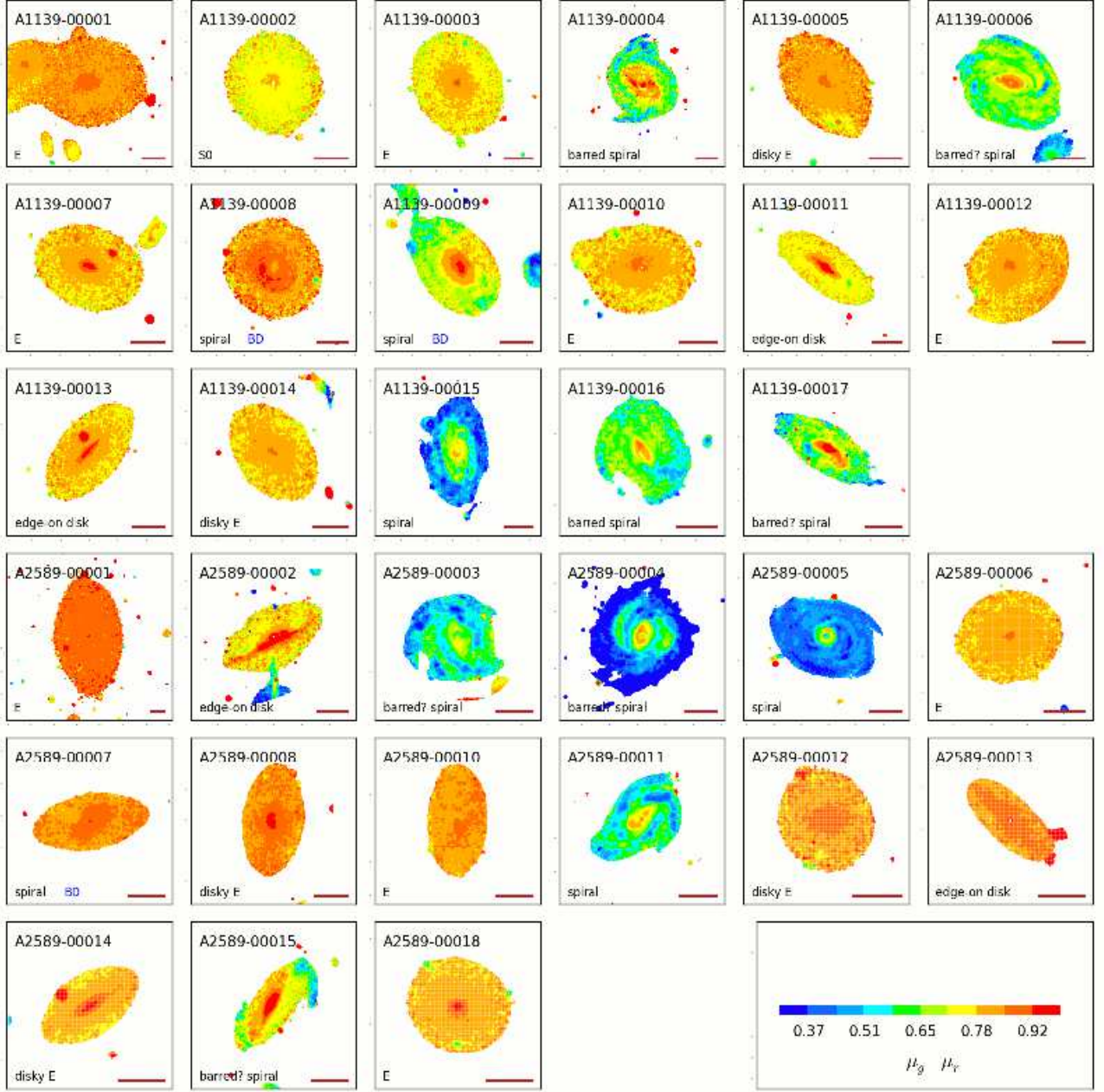


FIG. 5.— The $g - r$ color maps of the sample galaxies. The pixels fainter than $\mu_r = 23.2 \text{ mag arcsec}^{-2}$ are not plotted. The visually classified morphology and the 10 arcsec scale bar are also denoted.

In Lee et al. (2017), this procedure worked well, because the target galaxies were BCGs with relatively simple shapes and little complex substructures.

In this paper, on the other hand, the targets are galaxies in variety of morphology, from elliptical to spiral. Because elliptical galaxies (and most edge-on disk galaxies) do not show complex structures in their r -band images, there is no problem in applying the SE-detection-based masking to them. In the case of late-type galaxies, however, it does not work well to determine the masking apertures using the SE, because the SE hardly distinguish between contaminants (companions or foreground/background objects) and galaxy substructures (spiral arms, star-forming clumps, and bars). For a few late-type galaxies, the SE-detection-based masking re-

moves more than 80% of the entire image for a target galaxy, which is obviously over-masking.

Thus, we apply the SE-detection-based masking adaptively according to the target morphology and the masking performance. That is, the full procedure is applied if the SE-detection-based masking does not cause over-masking (e.g., A1139-00003). On the other hand, if the SE-detection-based masking (step 2 and/or step 3 in the procedure) appears to over-mask the target galaxy, the masking step is omitted (e.g., A1139-00004). During this adaptation, we intended to minimize the omission of masking. That is, the masking step is omitted only when it obviously over-masks the target galaxy, whereas the masking is conducted when it is unclear whether the target is over-masked or not. At least among our sample

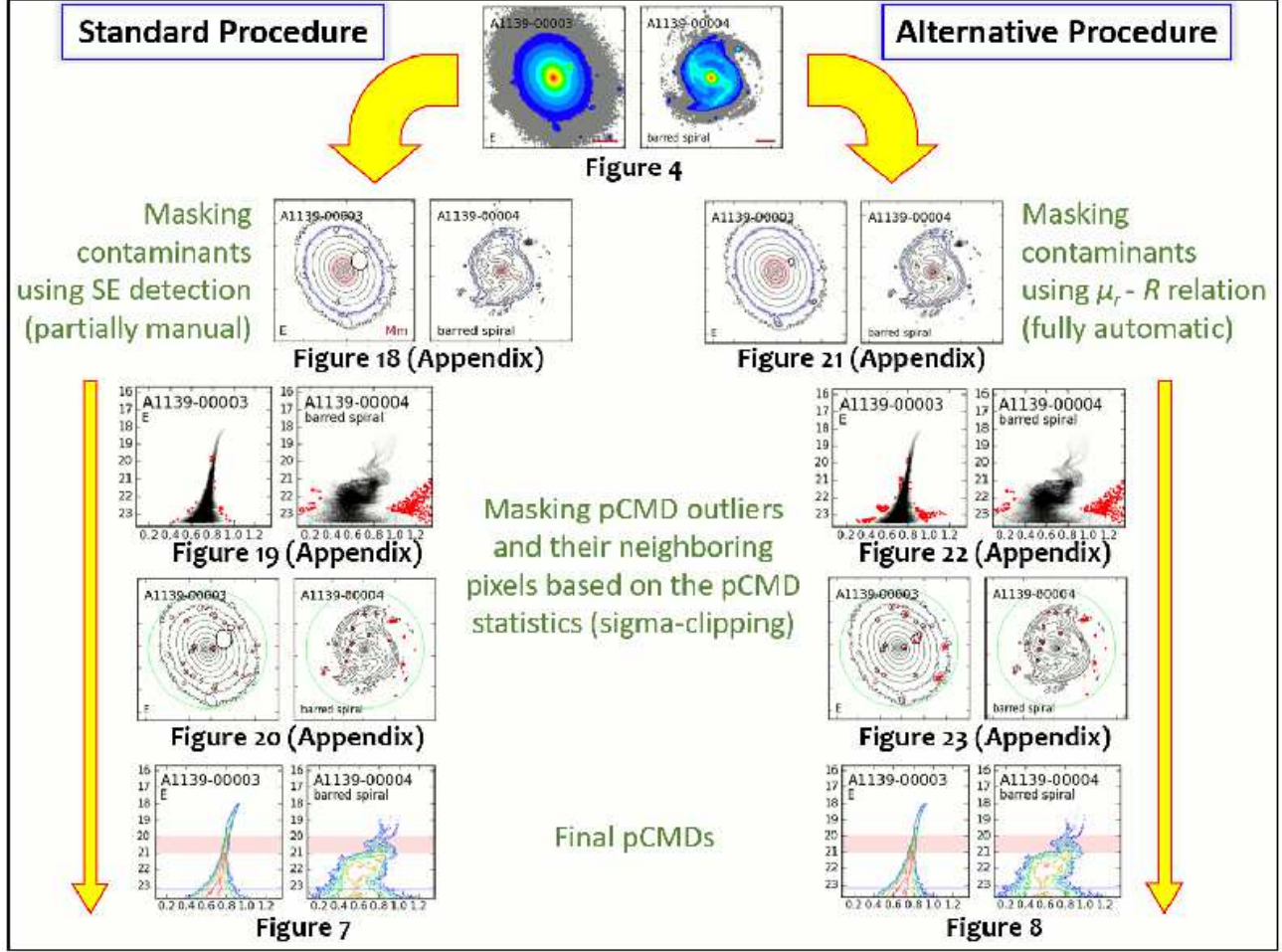


FIG. 6.— Schematic summary of the standard and alternative procedures. The left-side sequence shows the standard procedure (described in Section 3.1), while the right-side sequence shows the alternative procedure (described in Section 3.2). The full plots for the whole sample galaxies in each masking process are presented in Appendix A.

galaxies, there was rarely ambiguous situation and thus we decided the final masking sets relatively at ease.

However, the adaptive masking has a fundamental weakness: late-type galaxies with complicated structures tend to be masked too little, compared to early-type galaxies with simple structures. Because late-type galaxies are expected to have remaining contaminants that were not sufficiently masked in the SE-detection-based masking process, a supplementary masking process is necessary. For this, we additionally masked the pixels that correspond to the pCMD outliers. The processes are listed as follows:

1. Estimate the 5, 50, and 95 percentiles in the pixel $g-r$ color distribution at given μ_r , using the pCMD after the SE-detection-based masking,
2. Define $\sigma_1 \equiv (g-r)_{50\%} - (g-r)_{5\%}$ and $\sigma_2 \equiv (g-r)_{95\%} - (g-r)_{50\%}$ as a function of μ_r ,
3. Define pCMD outliers as the pixels with $g-r < (g-r)_{50\%} - 2\sigma_1$ or $g-r > (g-r)_{50\%} + 2\sigma_2$, at given μ_r , and
4. Mask the pCMD outliers and their neighboring pixels within $0.8''$ (seeing size).

Figure 6 schematically summarizes the entire masking procedures to yield the final pCMDs (the standard procedure at the left side). The plots at the second row of the left side in Figure 6 show the surface brightness contour maps of the sample galaxies after the adaptive (SE-detection-based) masking. The plots at the third row of the left side show the pCMDs after the SE-detection-based masking and the smoothing with the $0.8''$ -aperture spline kernel (Lee et al. 2017), with the pCMD outliers marked (see Appendix A for the full plots of the whole sample). The pCMD outliers of late-type galaxies mostly outnumber those of early-type galaxies, which means that many remaining contaminants in late-type galaxies are additionally masked in this process.

Note that the pCMD outlier masking is not perfect either. There may be still remaining contaminants or to the contrary there may be some over-masking particularly for fine substructures in the target galaxies. For example, the BCG of A2589 (A2589-00001) is thought to have vestiges of infalling low-mass star-forming satellites, which was revealed from the analysis of its pCMD outliers in Lee et al. (2017). Such fine features are mostly washed out in the pCMD outlier masking process. Thus, this process can not be used if we want to inspect the fine substructures in target galaxies. However, it does not significantly affect the main features of the pCMD

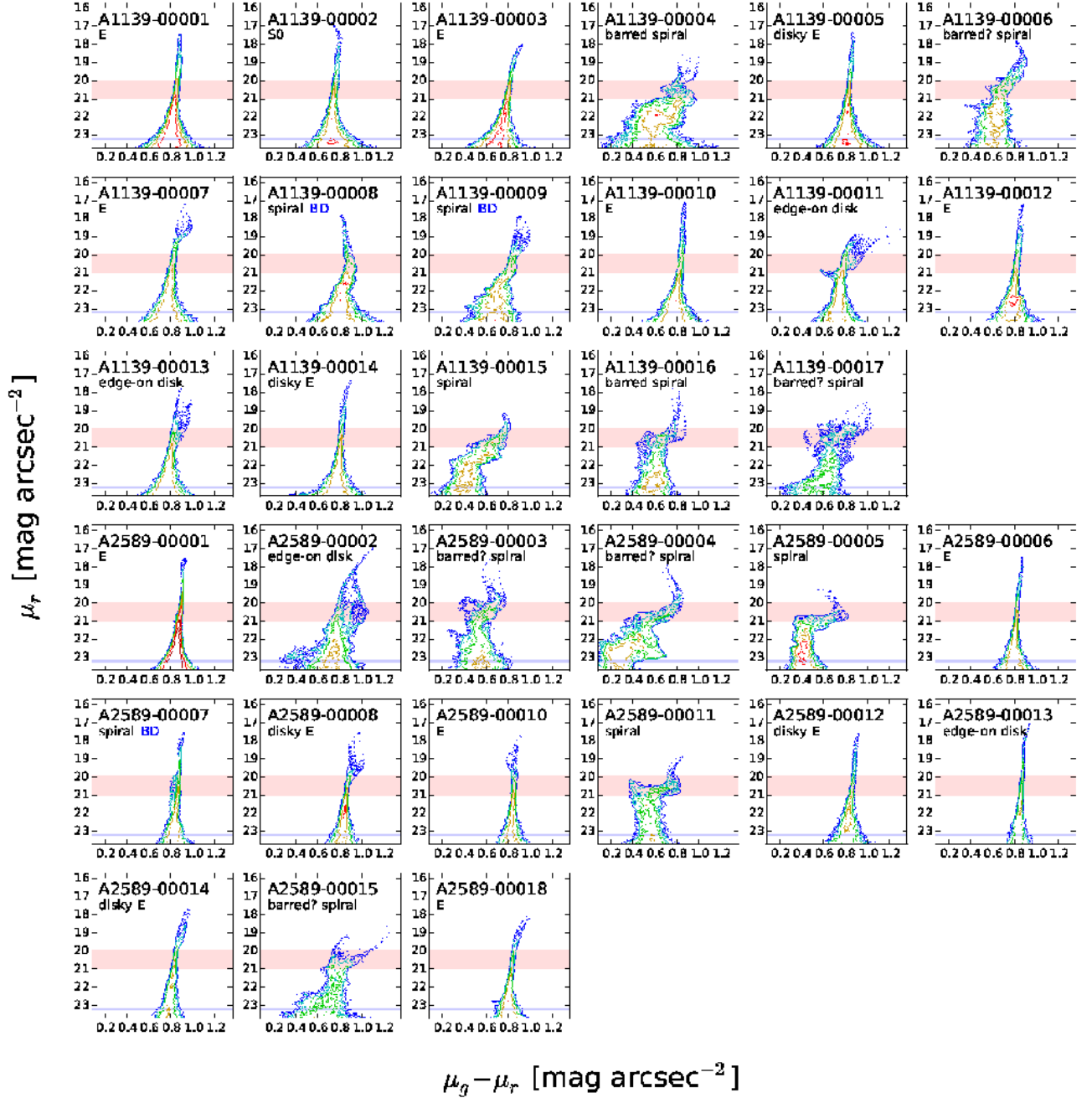


FIG. 7.— The log-scale pixel number density contours of the final pCMDs after the standard masking procedure. The $20.0 \leq \mu_r \leq 21.0$ mag arcsec $^{-2}$ range (faint red stripe) and the $\mu_r = 23.2$ mag arcsec $^{-2}$ limit (faint blue line) are denoted.

backbones, because the number of the outliers are typically much smaller than that of the pixels in main features. The plots at the fourth row in Figure 6 present the μ_r contour maps after masking pCMD outliers and their neighboring pixels within $0.8''$. After these two-step masking processes, the final pCMDs are yielded as shown in Figure 7.

3.2. Alternative Procedure

In the standard procedure, the SE-detection-based masking process for contaminants has two weaknesses. One is that late-type galaxies can not be sufficiently masked using the SE-detection-based method, which is supplemented to some extent using the pCMD outlier

masking as described in Section 3.1. However, another weakness still remains: the ‘adaptive masking’ can cause a bias when we compare the pCMD properties between different morphological types. As already mentioned, late-type galaxies tend to be less suitable for the SE-detection-based masking than early-type galaxies. Among the 13 spiral galaxies, the SE-detection-based masking is completely omitted for four spirals (A1139-00004, A2589-00003, A2589-00004, and A2589-00011), while the full masking processes are applied to only two spirals (A1139-00008 and A2589-00007). On the other hand, the full masking processes were applied to every elliptical galaxy. That is, the masking processes for early- and late-type galaxies are not identical in the standard

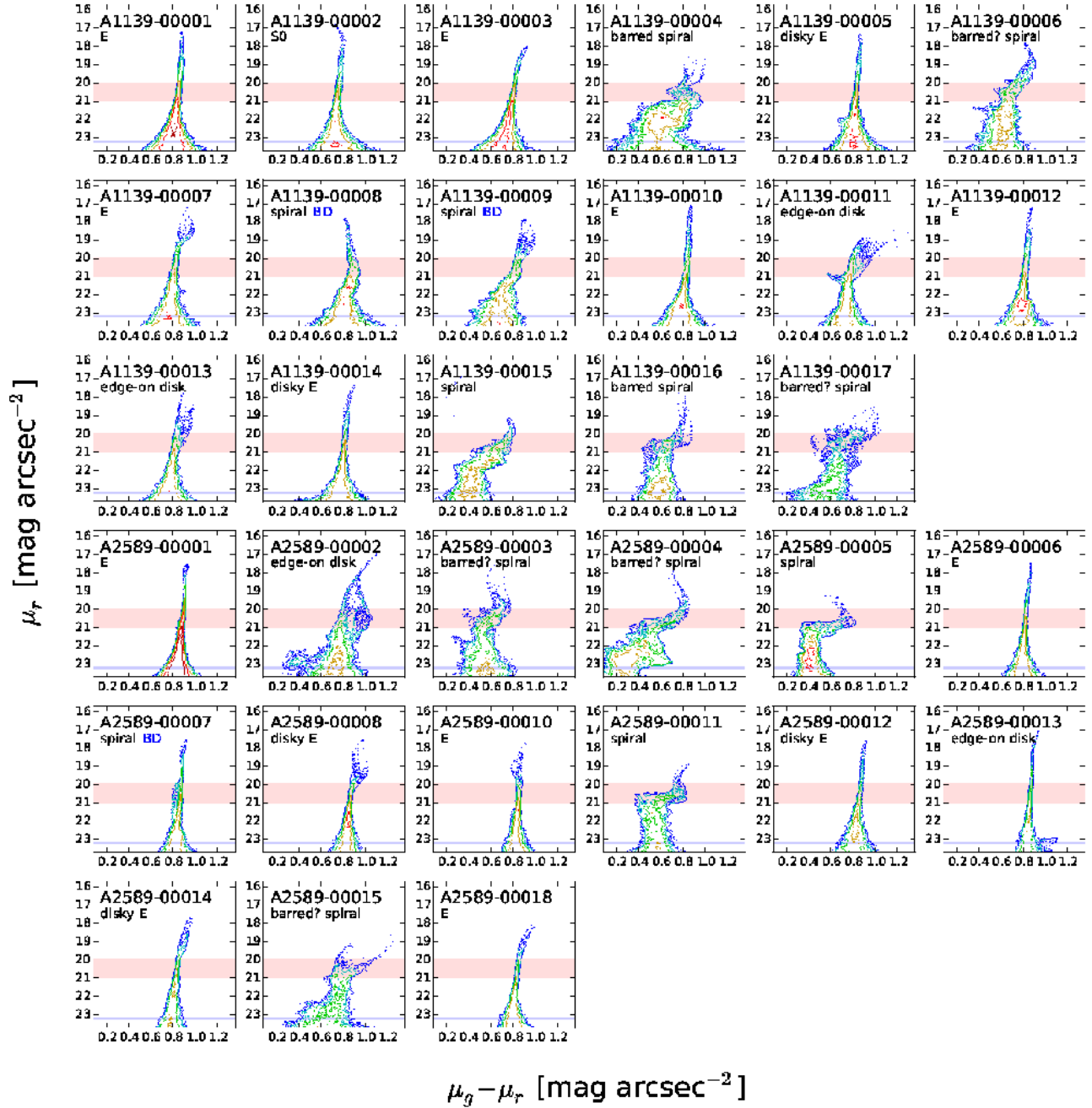


FIG. 8.— The log-scale pixel number density contours of the final pCMDs after the alternative masking procedure. The $20.0 \leq \mu_r \leq 21.0$ mag arcsec $^{-2}$ range (faint red stripe) and the $\mu_r = 23.2$ mag arcsec $^{-2}$ limit (faint blue line) are denoted.

procedure, and thus the comparison of the final pCMDs between galaxies with different morphological types may not be fair.

To address this issue, we try an alternative masking procedure that does not depend on subjective ‘adaptation’ according to galaxy morphology. This procedure is based on the idea that the light from contaminants tends to be brighter than the brightness expected at the distance from the target galaxy center. The detailed procedure is as follows:

1. Trim a sufficient area around a target galaxy,
2. Trim the image again with a radius of $f_c \times R_{80(22.2-23.2)}$, where f_c is a fixed value and

$R_{80(22.2-23.2)}$ is the 80 percentile in the distribution of distance to center, among pixels with $22.2 \leq \mu_r \leq 23.2$ mag arcsec $^{-2}$; we empirically choose $f_c = 1.5$ (see Appendix A for the trimming area for each sample galaxy),

3. Estimate the 10 and 50 percentiles in the distribution of distance to center, among pixels with given μ_r ($R_{10_{\mu_r}}$ and $R_{50_{\mu_r}}$, respectively),
4. Mask pixels with μ_r and radial distance (R) satisfying $R - R_{10_{\mu_r}} > f_R \times (R_{50_{\mu_r}} - R_{10_{\mu_r}})$, where we empirically choose $f_R = 5$, and
5. Conduct the additional pCMD outlier masking as

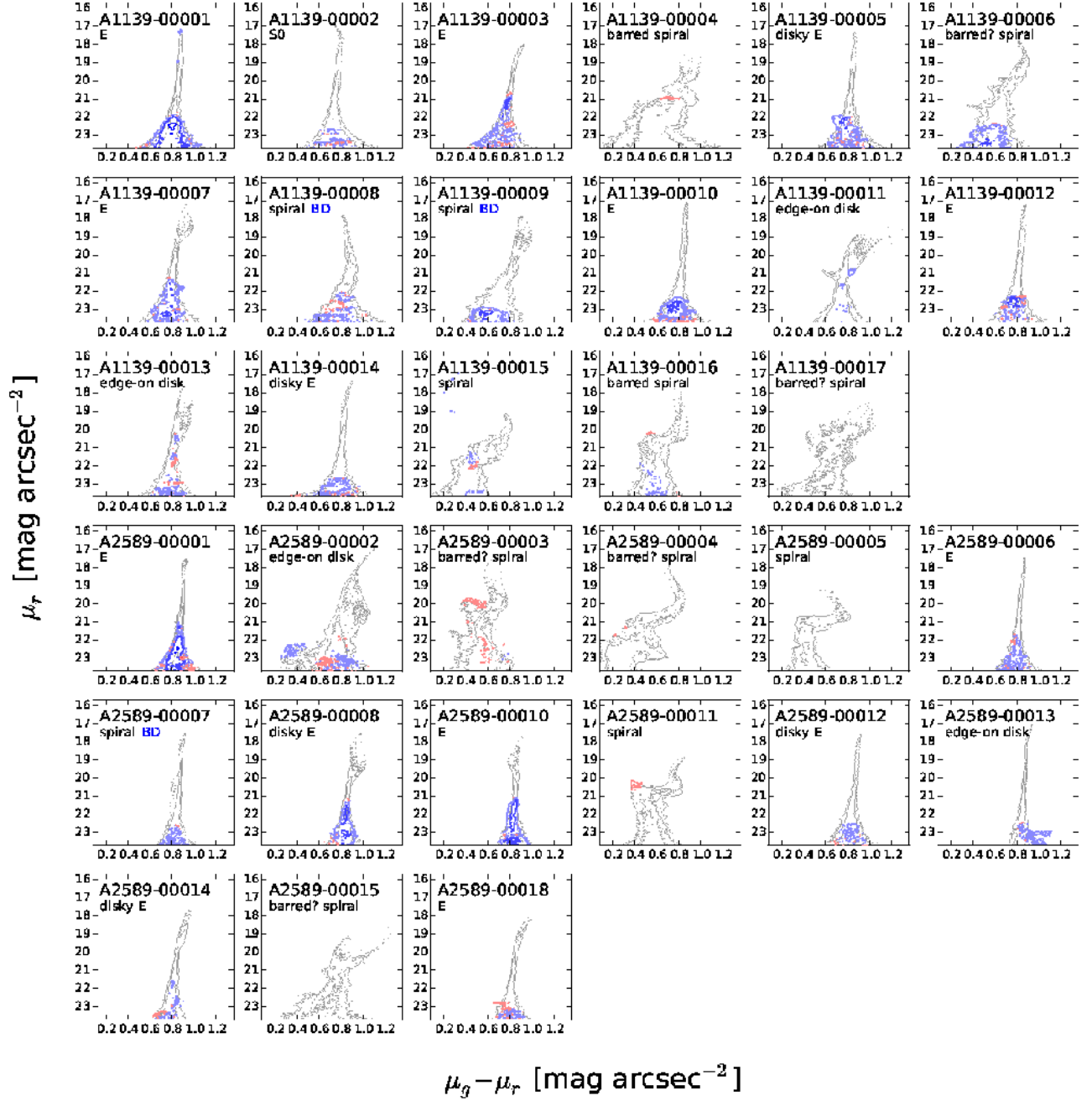


FIG. 9.— The log-scale contours of the difference in pixel number density of pCMDs between the two masking procedures (Figure 7 subtracted by Figure 8). The red contours indicate the domain at which the pCMDs after the standard masking procedure are denser (Figure 7 > Figure 8), whereas the blue contours show the opposite cases (Figure 7 < Figure 8). The gray contours show the pCMDs after the standard masking procedure.

described in Section 3.1.

These processes depend on a few control parameters empirically determined, which is a weakness. Nevertheless, this method has a considerable merit: it can be consistently applied to target galaxies regardless of their morphological types.

The plots at the second row of the right side in Figure 6 show the surface brightness contour maps after this μ_r -radius-relation-based ($R(\mu_r)$ -based) masking. The overall area masked by the $R(\mu_r)$ -based method tends to be smaller (under-masking) than that by the SE-detection-based method. Thus, the role of the pCMD outlier mask-

ing is more important in the alternative procedure, because it supplements the weak performance of the $R(\mu_r)$ -based masking. In this procedure, on the other hand, the number of pCMD outliers is averagely not so different between early- and late-type galaxies, unlike that in the standard procedure. This is because the alternative masking procedure is free from the morphology bias caused by subjective ‘adaptation’.

The final pCMDs after the alternative masking procedure are presented as pixel number density contours in Figure 8. The overall features of the pCMDs in Figure 8 are not significantly different from those after the

TABLE 2
PARAMETERS DESCRIBING pCMD FEATURES

| pCMD Parameter | Description |
|---|---|
| $\mu_r(\text{tip})$ | Minimum (brightest) r -band surface brightness among all pixels |
| $\min(g-r)_{\mu_r \leq 23.2}$ | Minimum (bluest) value of mean $g-r$ color at $\mu_r \leq 23.2 \text{ mag arcsec}^{-2}$ |
| $\max(g-r)_{\mu_r \leq 23.2}$ | Maximum (reddest) value of mean $g-r$ color at $\mu_r \leq 23.2 \text{ mag arcsec}^{-2}$ |
| $\min(\sigma(g-r))_{\mu_r \leq 21.2}$ | Minimum (tightest) value of $g-r$ color dispersion at $\mu_r \leq 21.2 \text{ mag arcsec}^{-2}$ |
| $\max(\sigma(g-r))_{\mu_r \leq 21.2}$ | Maximum (most dispersed) value of $g-r$ color dispersion at $\mu_r \leq 21.2 \text{ mag arcsec}^{-2}$ |
| $\max(\sigma(g-r))_{20.0 \leq \mu_r \leq 21.0}$ | Maximum value of $g-r$ color dispersion at $20.0 \leq \mu_r \leq 21.0 \text{ mag arcsec}^{-2}$ |
| $\max(\sigma(g-r))_{18.5 \leq \mu_r \leq 19.5}$ | Maximum value of $g-r$ color dispersion at $18.5 \leq \mu_r \leq 19.5 \text{ mag arcsec}^{-2}$ |

NOTE. — The ‘mean $g-r$ color’ and ‘ $g-r$ color dispersion’ indicate the quantities estimated using the pixels with fixed μ_r . That is, $\min(g-r)_{\mu_r \leq 23.2}$ is the bluest value among the ‘mean $g-r$ colors as a function of μ_r ’, not the $g-r$ color of the bluest pixel among the whole pixels. In the text, ‘the minimum (maximum) $g-r$ color’ indicates ‘the minimum (maximum) value of mean $g-r$ color as a function of μ_r ’.

standard masking procedure in Figure 7, but some small details appear to be in disagreement. Such differences are revealed in Figure 9, which shows the pixel number density contours for the pCMD residuals (Figure 7 subtracted by Figure 8). In most cases, the pixels in the pCMDs after the alternative procedure outnumber those after the standard procedure (blue contours). This means that the alternative procedure is less efficient in masking contaminants than the standard procedure at least for early-type galaxies. On the other hand, the opposite case is much rarer (red contours) even for late-type galaxies. It is hard to increase the masking efficiency of the alternative procedure by adjusting f_R , because a too small f_R value frequently results in unreasonable masking.

In summary, the alternative procedure is not sufficiently good in the aspect of masking efficiency, but the results from the alternative procedure are necessary when technically fair comparison without any morphology bias is required. In Section 4, we mainly analyze the results from the standard procedure, to take an advantage of its masking efficiency (mainly for early-type galaxies). However, the results from the alternative procedure are also used to check the effect of morphology bias, which are fully presented in Appendix B.

4. RESULTS

4.1. Overall Description of the pCMDs

In the final pCMDs (Figures 7 and 8), early-type galaxies show simple pCMD features, whereas late-type galaxies show significantly curved pCMDs. As introduced in Section 1, those features are called prime sequences and inverse-L features in Lanyon-Foster et al. (2007), respectively. However, such a dichotomic division is not always obvious. Some early-type galaxies have considerably disturbed features at their bright parts (A1139-00007, A2589-00008 and A2589-00014), and besides the pCMDs of some bulge-dominated late-type galaxies or edge-on disk galaxies are similar to those of early-type galaxies (A2589-00007 and A2589-00013). That is, galaxies even in similar morphological types have variety in their pCMD features, and such variety is larger in late-type galaxies.

In the case of early-type galaxies, the unusual features (deviated from the prime sequences) seem to be closely related to tidal interactions with nearby neighbors or companions. The prime sequences of the elliptical galax-

ies show curvatures different from one another, which implies that their formation histories are not entirely homologous as discussed in Lee et al. (2017). Different internal dust extinction may be responsible for such variety, too (Lee et al. 2011, 2012). The only face-on S0 galaxy in our sample (A1139-00002) shows a blue pCMD-tip feature, which indicates that this galaxy may have experienced central star formation activity very recently.

The (barred and unbarred) spiral galaxies show complex and diverse features in their pCMDs. The pCMD structures of a spiral galaxy is roughly described to consist of a (red and bright) bulge part and a (blue and faint) disk part, which form an overall inverse-L feature. However, whereas this division is quite clear in some spiral galaxies (A1139-00016, A2589-00004 and A2589-00011), some other spiral galaxies show more complicated and amorphous features (A1139-00017 and A2589-00015). The bulge-dominated spiral galaxies (A1139-00008, A1139-00009 and A2589-00007) show relatively simple pCMD features compared to the other spiral galaxies, but more distorted than the pCMDs of typical elliptical galaxies.

Finally, some edge-on disk galaxies (A1139-00013 and A2589-00013) have pCMDs similar to those of elliptical galaxies, but some other edge-on disk galaxies do not (A1139-00011 and A2589-00002). The former edge-on disk galaxies have quite elliptical appearances in their r -band images (Figure 3), but they were classified into edge-on disks because an edge-on dust lane is found (A1139-0013) or the morphology is too elongated to be an elliptical galaxy (A2589-00013). The latter edge-on disks are clearly different from elliptical galaxies in their appearances.

4.2. Quantitative Comparison

One of the main purposes of this paper is to establish a quantitative method using pCMDs to distinguish between galaxies with different morphological types. For quantitative comparison of the pCMD features, we devised several parameters describing the features of pCMDs as listed in Table 1.

4.2.1. Reliability Limits

Following Lee et al. (2017), we limit our analysis to $\mu_r \leq 23.2 \text{ mag arcsec}^{-2}$ for the use of pixel color, at which the photometric uncertainty of a single pixel is smaller than $0.03 \text{ mag arcsec}^{-2}$. On the other hand, the

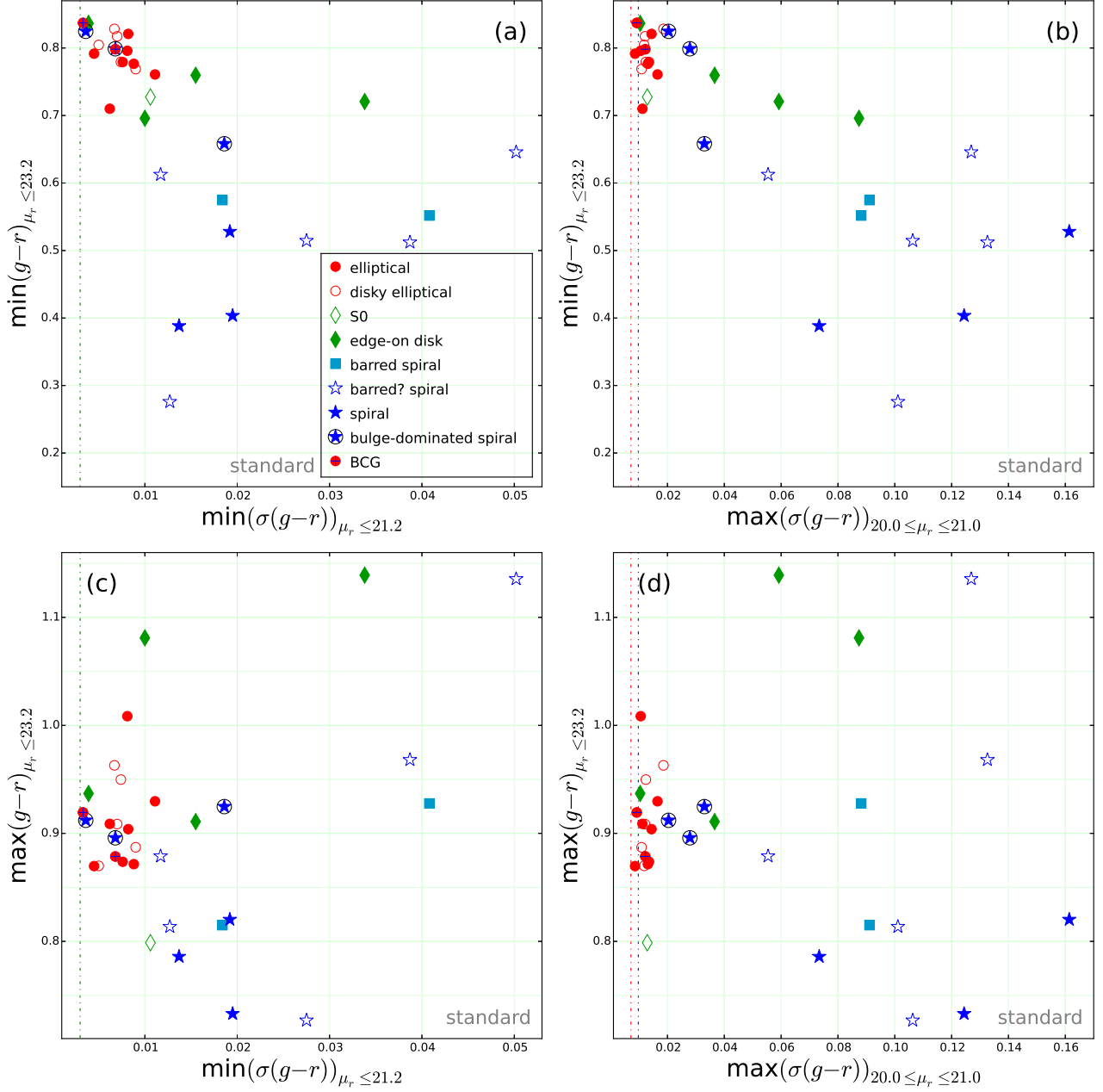


FIG. 10.— Correlations between pCMD parameters, based on the pCMDs after the standard procedure: (a) the minimum $g-r$ color at $\mu_r \leq 23.2$ mag arcsec $^{-2}$ versus the minimum $g-r$ color dispersion at $\mu_r \leq 21.2$ mag arcsec $^{-2}$, (b) the minimum $g-r$ color at $\mu_r \leq 23.2$ mag arcsec $^{-2}$ versus the maximum $g-r$ color dispersion at $20.0 \leq \mu_r \leq 21.0$ mag arcsec $^{-2}$, (c) the maximum $g-r$ color at $\mu_r \leq 23.2$ mag arcsec $^{-2}$ versus the minimum $g-r$ color dispersion at $\mu_r \leq 21.2$ mag arcsec $^{-2}$, and (d) the maximum $g-r$ color at $\mu_r \leq 23.2$ mag arcsec $^{-2}$ versus the maximum $g-r$ color dispersion at $20.0 \leq \mu_r \leq 21.0$ mag arcsec $^{-2}$. The dot-dashed lines represent the lower limits of color dispersion, above which color dispersion is dominated by intrinsic color scatter rather than photometric uncertainty, at 21.0 mag arcsec $^{-2}$ for A1139 (blue; in panels (b) and (d)), at 21.0 mag arcsec $^{-2}$ for A2589 (red; in panels (b) and (d)), and at 19.2 mag arcsec $^{-2}$ for both clusters (green; in panels (a) and (c)).

limit for the use of pixel color dispersion⁴ ($\sigma(g-r)$) is $\mu_r \leq 21.2$ mag arcsec $^{-2}$. At $\mu_r > 21.2$ mag arcsec $^{-2}$, color dispersion tends to be significantly affected by the photometric uncertainty of individual pixels and thus cannot represent the intrinsic scatter of pixel color (see

⁴ In this paper, the word ‘color dispersion’ indicates the standard deviation of pixel colors at given μ_r . This quantity was called ‘color deviation’ in Lee et al. (2017), but we replace it by ‘color dispersion’ for better understanding.

Figure 11 of Lee et al. 2017).

When we compare color dispersion values, the consideration of photometric uncertainty is important even at $\mu_r \leq 21.2$ mag arcsec $^{-2}$, depending on situation. Lee et al. (2017) empirically showed that the lower limit of reliable color dispersion at given μ_r is $1.3 \times$ photometric uncertainty of a single pixel in A1139 and A2589. For example, if a $\max(\sigma(g-r))_{20.0 \leq \mu_r \leq 21.0}$ value is close to the value of $1.3 \times$ typical photometric uncertainty at $\mu_r = 21.0$ mag arcsec $^{-2}$, then the measured

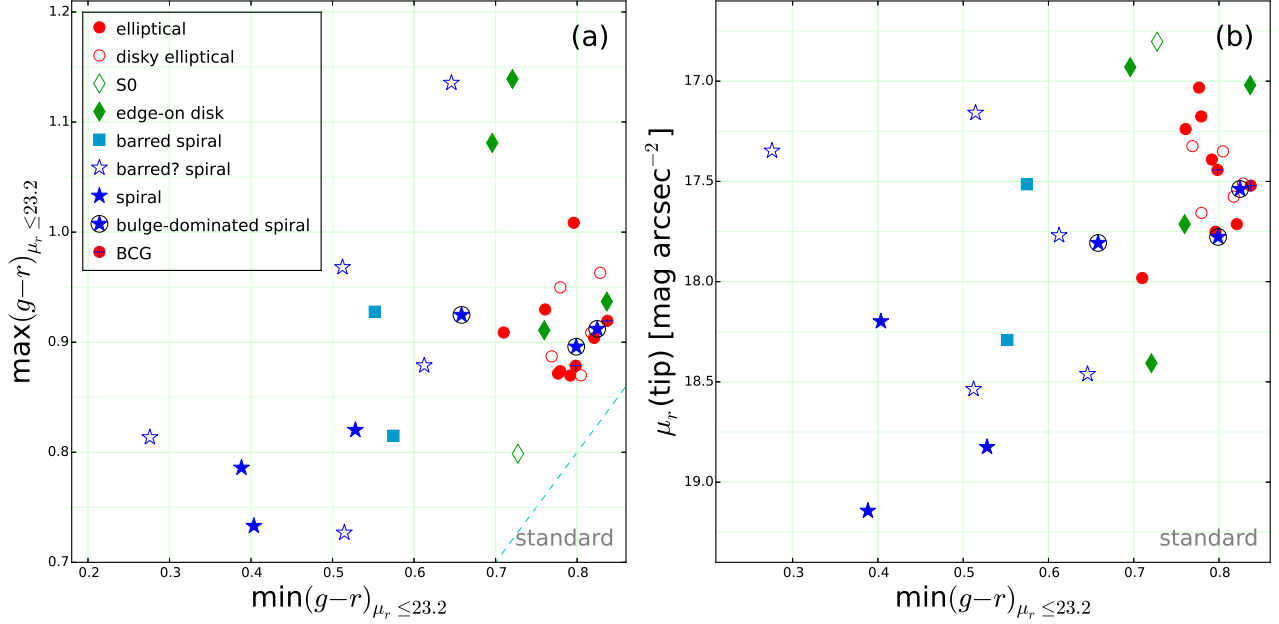


FIG. 11.— (a) The maximum versus minimum values of mean $g-r$ color at $\mu_r \leq 23.2$ mag arcsec $^{-2}$, and (b) the brightest μ_r versus the minimum $g-r$ color at $\mu_r \leq 23.2$ mag arcsec $^{-2}$, based on the pCMDs after the standard masking procedure. Various symbols indicate the morphological types, and the dashed line (cyan) shows the one-to-one relation.

$\max(\sigma(g-r))_{20.0 \leq \mu_r \leq 21.0}$ value indicates the upper limit rather than the intrinsic color dispersion. In other words, we can regard the color dispersion to be intrinsic only when the value is sufficiently larger than $1.3 \times$ photometric uncertainty.

This should be also considered when we compare $\min(\sigma(g-r))_{\mu_r \leq 21.2}$. Although the minimum color dispersion usually corresponds to the color dispersion at the brightest μ_r ($\mu_r(\text{tip})$) and the photometric uncertainty of the brightest pixel is typically tiny, the reliability limit needs to be counted if the measured color dispersion is also very small. Because the faintest surface brightness among the brightest pixels of our sample galaxies (i.e., maximum $\mu_r(\text{tip})$) is about 19.2 mag arcsec $^{-2}$, we can safely regard the $\min(\sigma(g-r))_{\mu_r \leq 21.2}$ value to be intrinsic if it is larger than $1.3 \times$ photometric uncertainty at $\mu_r = 19.2$ mag arcsec $^{-2}$. In the subsequent investigation, all interpretations of the figures are based on these considerations.

4.2.2. Galaxy Morphology and pCMD Parameters

From now on, we investigate the relationship between the pCMD parameters and galaxy morphology, and its physical implication. Figure 10 presents the basic correlations between the pCMD parameters, with the morphological types denoted. The trends between the parameters in the whole sample are mostly not obvious, but Figure 10(b) shows a notable anti-correlation between $\min(g-r)_{\mu_r \leq 23.2}$ and $\max(\sigma(g-r))_{20.0 \leq \mu_r \leq 21.0}$. This anti-correlation appears to be closely related with galaxy morphology, in the context that elliptical galaxies tend to have larger $\min(g-r)_{\mu_r \leq 23.2}$ and smaller $\max(\sigma(g-r))_{20.0 \leq \mu_r \leq 21.0}$ than the galaxies with the other types. This is a quantitative expression of the fact that the elliptical galaxies hardly have blue pixels and their pCMDs tend to be tightly bound.

A similar plot was shown in Figure 13 of Lanyon-Foster

et al. (2007), in which the mean pixel color and the mean pixel color dispersion were compared. Although Lanyon-Foster et al. (2007) found a correlation between those mean values, its scatter is larger than that in our Figure 10(b). This indicates that the minimum pixel color and the maximum pixel color dispersion are better indicators of galaxy morphology than the mean values. On the other hand, the minimum pixel color dispersion (Figure 10(a)) or the maximum pixel color (Figure 10(c)-(d)) seems to be less efficient even than the mean values. The reason is not difficult to figure out: even late-type galaxies may have small $\min(\sigma(g-r))$ values owing to their bulges, and large $\max(g-r)$ values due to significant dust extinction in their disks as well as bulges.

In Figure 11, we examine how well galaxy morphology is distinguished by pCMD colors and $\mu_r(\text{tip})$. In Figure 11(a), the elliptical galaxies are distributed in a small domain, whereas the spiral galaxies show a much wider distribution. Most spiral galaxies tend to have pixel colors bluer than those of early-type galaxies, but the $\max(g-r)_{\mu_r \leq 23.2}$ values of some late-type galaxies are similar to those of early-type galaxies (A1139-00017 and A1139-00006) or even larger (A2589-00015). On the other hand, $\min(g-r)_{\mu_r \leq 23.2}$ seems to divide elliptical galaxies from spiral galaxies better than $\max(g-r)_{\mu_r \leq 23.2}$ does, except for bulge-dominated spiral galaxies (A1139-00008 and A2589-00007) and edge-on disk galaxies. These are because $\max(g-r)_{\mu_r \leq 23.2}$ represents the color of a late-type galaxy's bulge which is known to be similar to an elliptical galaxy in their properties (Dressler 1987; Fisher & Drory 2008)⁵, whereas $\min(g-r)_{\mu_r \leq 23.2}$ is strongly affected by their disk parts. In Figure 11(b), the $\mu_r(\text{tip})$ is brighter than 18.0 mag arcsec $^{-2}$ for all elliptical galaxies in our sample. On the other hand, many spiral galaxies have fainter $\mu_r(\text{tip})$, but

⁵ But, see also Gadotti (2009).

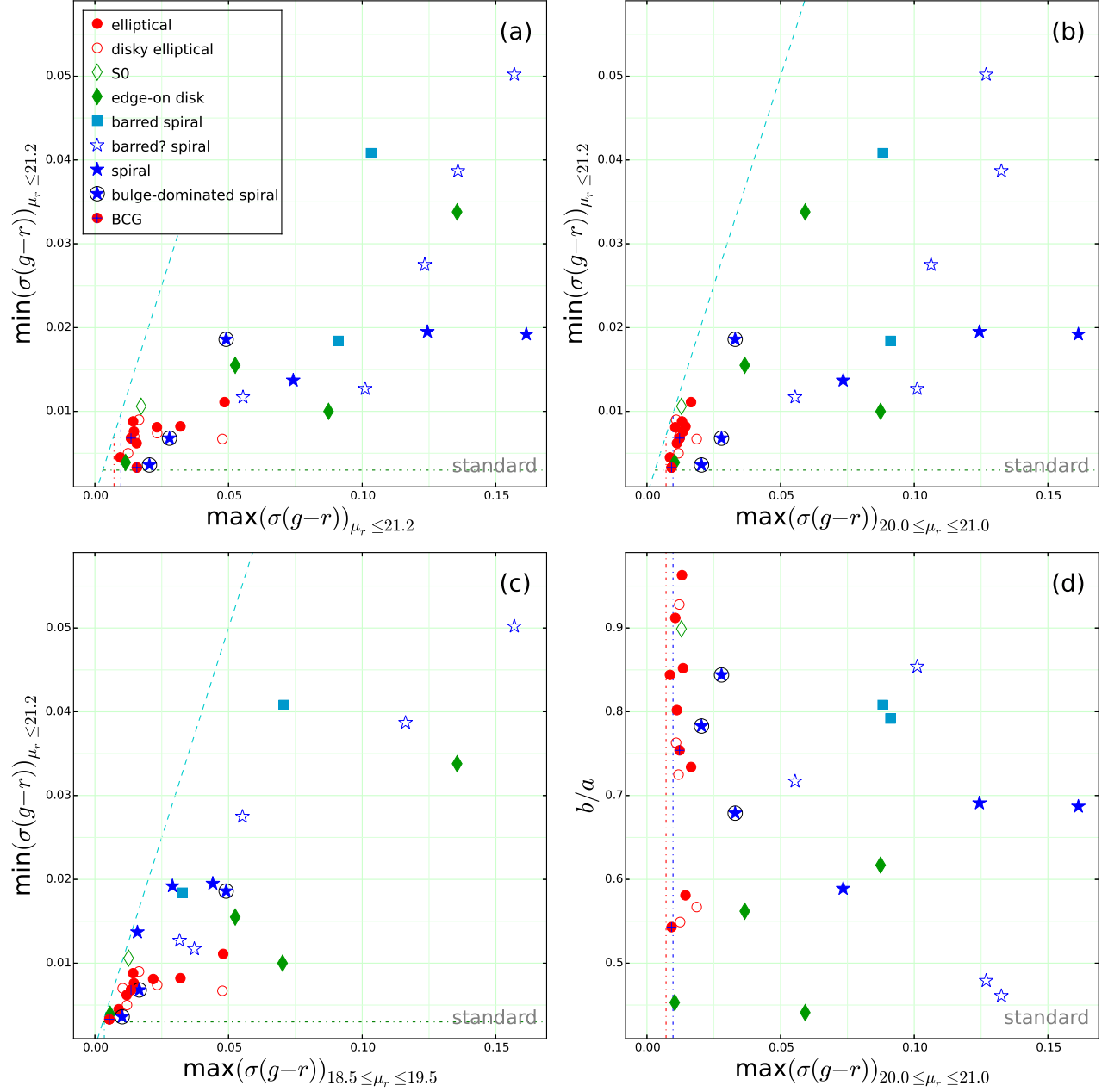


FIG. 12.— The minimum $g-r$ color dispersion at $\mu_r \leq 21.2$ mag arcsec $^{-2}$ (a) versus the maximum $g-r$ color dispersion at $\mu_r \leq 21.2$ mag arcsec $^{-2}$, (b) versus the maximum $g-r$ color dispersion at $20.0 \leq \mu_r \leq 21.0$ mag arcsec $^{-2}$, and (c) versus the maximum $g-r$ color dispersion at $18.5 \leq \mu_r \leq 19.5$ mag arcsec $^{-2}$. (d) Axis ratio versus the maximum $g-r$ color dispersion at $20.0 \leq \mu_r \leq 21.0$ mag arcsec $^{-2}$. The dashed lines (cyan) show the one-to-one relations. The blue, red and green dot-dashed lines are the reliability limits as described in Figure 10, and the cyan vertical dot-dashed line in Panel (c) is the lower limit at 19.5 mag arcsec $^{-2}$ for both clusters. All parameters are based on the pCMDs after the standard masking procedure.

some spiral galaxies have $\mu_r(\text{tip})$ as bright as those of elliptical galaxies (A2589-00003 and A2589-00004). These results show that the combination of pCMD colors and $\mu_r(\text{tip})$ moderately divides early- and late-type galaxies, but not perfectly.

Next, we test the capability of pCMD color dispersion parameters to classify galaxy morphology, in Figure 12. The combination of color dispersion divides early- and late-type galaxies as nicely as or even better than the color index combination does. This indicates that the complexity of stellar populations at given μ_r as well as

their mean age and metallicity is an important feature discriminating between early- and late-type galaxies. After examining various combinations, we found that the best combination to discriminate galaxy morphology is $\min(\sigma(g-r))_{\mu_r \leq 21.2}$ and $\max(\sigma(g-r))_{20.0 \leq \mu_r \leq 21.0}$. In Figure 12(b) (zoomed-in in Figure 13(a)), the elliptical galaxies are well separated from the spiral galaxies, even from the bulge-dominated spiral galaxies unlike in Figure 11. This seems to be mainly because $\max(\sigma(g-r))_{20.0 \leq \mu_r \leq 21.0}$ represents how complex the stellar populations are at the region where the disk com-

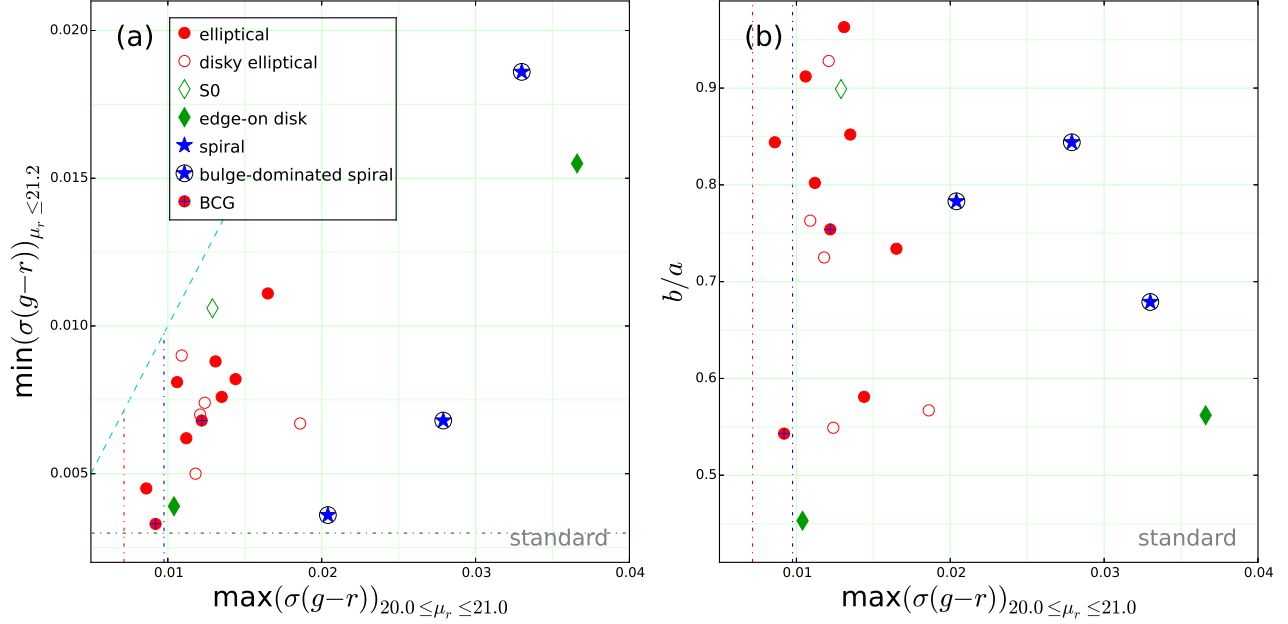


FIG. 13.— Zoom-in plots of (a) the minimum $g-r$ color dispersion at $\mu_r \leq 21.2$ mag arcsec $^{-2}$ versus the maximum $g-r$ color dispersion at $20.0 \leq \mu_r \leq 21.0$ mag arcsec $^{-2}$ (Figure 12(b)), and (b) axis ratio versus the maximum $g-r$ color dispersion at $20.0 \leq \mu_r \leq 21.0$ mag arcsec $^{-2}$ (Figure 12(d)). Both of the plots are based on the pCMDs after the standard masking procedure.

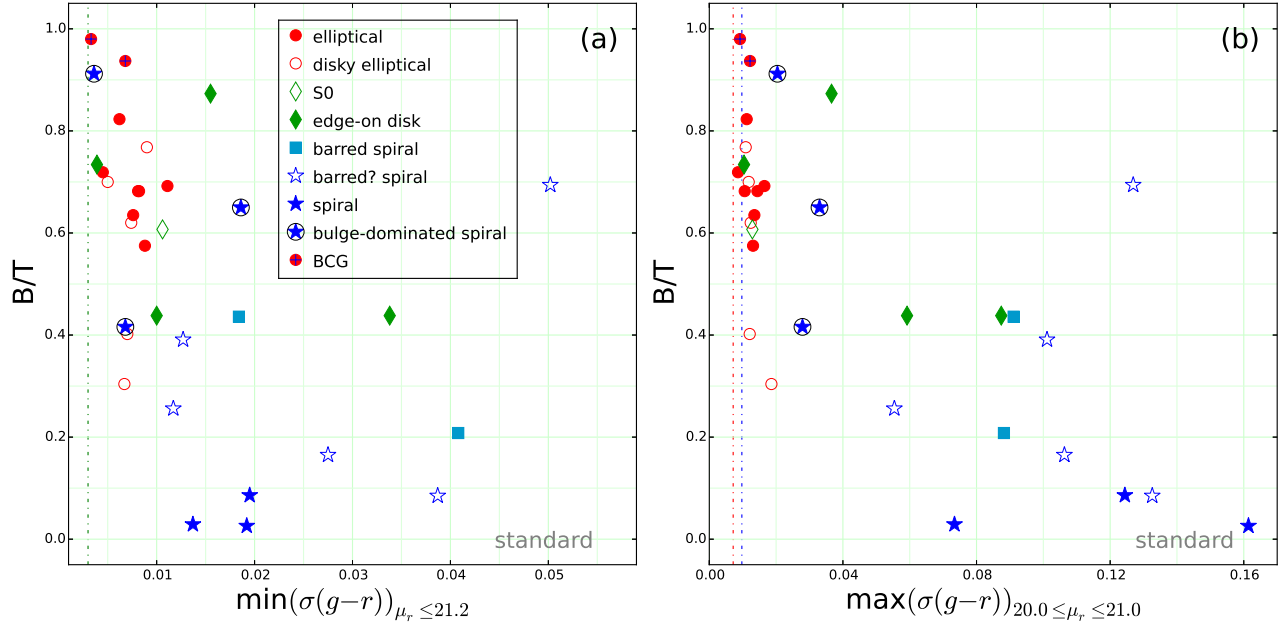


FIG. 14.— Comparison with bulge-to-total ratio (B/T) of (a) minimum $g-r$ color dispersion at $\mu_r \leq 21.2$ mag arcsec $^{-2}$ and (b) maximum $g-r$ color dispersion at $20.0 \leq \mu_r \leq 21.0$ mag arcsec $^{-2}$.

ponent starts to surpass the bulge component in a typical late-type galaxy. It consequently reflects the disk dominance in a galaxy, because stellar populations in a disk tend to be much more complex than those in a bulge. See the plots at the second row in Figure 6 (and Appendix A) for the spatial areas covered by the pixels with $20.0 \leq \mu_r \leq 21.0$ in each galaxy.

However, although the $\min(\sigma(g-r))_{\mu_r \leq 21.2}$ versus $\max(\sigma(g-r))_{20.0 \leq \mu_r \leq 21.0}$ plot seems to distinguish early-type (E, disk E and S0) galaxies from spiral galaxies al-

most perfectly, the edge-on disk galaxies are still mixed with the elliptical galaxies in this plot. To distinguish them, a parameter that is not from a pCMD is necessary: the axis ratio (b/a). Figure 12(d) (zoomed-in in Figure 13(b)) shows that the edge-on disk galaxies are separated from the early-type galaxies in the b/a versus $\max(\sigma(g-r))_{20.0 \leq \mu_r \leq 21.0}$ plot, due to their small b/a values. In summary, at least in our sample, the early-type galaxies are well distinguished from the other galaxies in the parameter space of $\min(\sigma(g-r))_{\mu_r \leq 21.2}$,

TABLE 3
CORRELATIONS WITH THE WISE [4.6] – [12] COLOR

| pCMD Parameters | All | E | E + disk | E | Spirals |
|---|---------------|--------------|--------------|---------------|---------|
| $\min(g-r)_{\mu_r \leq 23.2}$ | -0.87 (0.000) | 0.03 (0.935) | 0.19 (0.506) | -0.62 (0.052) | |
| $\max(g-r)_{\mu_r \leq 23.2}$ | -0.25 (0.173) | 0.37 (0.330) | 0.54 (0.044) | -0.72 (0.019) | |
| $\min(\sigma(g-r))_{\mu_r \leq 21.2}$ | 0.64 (0.000) | 0.66 (0.052) | 0.37 (0.190) | -0.44 (0.199) | |
| $\max(\sigma(g-r))_{20.0 \leq \mu_r \leq 21.0}$ | 0.86 (0.000) | 0.80 (0.010) | 0.77 (0.001) | 0.19 (0.602) | |

NOTE. — Pearson correlation coefficients (and p-values) with the WISE [4.6] – [12] color, for all galaxies (All; 32), elliptical galaxies (E; 9), elliptical + disk elliptical galaxies (E + disk; 14), and barred + unbarred spiral galaxies (Spirals; 13), based on the pCMDs after the standard masking procedure.

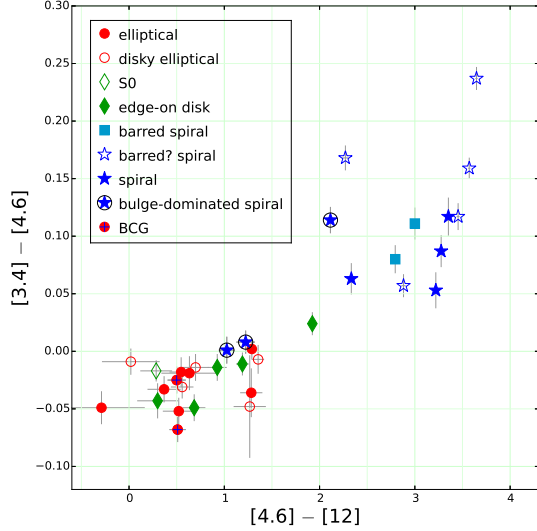


FIG. 15.— WISE infrared color-color diagram of the sample galaxies. Photometric uncertainties are denoted as gray lines for each target.

$\max(\sigma(g-r))_{20.0 \leq \mu_r \leq 21.0}$, and axis ratio. The pCMDs from the alternative masking procedure also give consistent results (Appendix B).

In Figure 14, we compare the pCMD color dispersion parameters with B/T, one of the most frequently used indicators of galaxy morphology. The performance of B/T for morphological classification is not bad: the elliptical and spiral galaxies are mostly separated by B/T. However, B/T fails to distinguish between elliptical galaxies and bulge-dominated spiral galaxies. Since $\max(\sigma(g-r))_{20.0 \leq \mu_r \leq 21.0}$ even distinguishes between the elliptical galaxies and bulge-dominated galaxies, the performance of B/T appears to be poorer than the color dispersion. Note that the structural decomposition may be improved if one makes more efforts, such as more careful setup of masks and initial guess, and more various component-functions for more realistic fitting (Peng et al. 2010; Kim et al. 2016). However, such a possibility of improvement in structural decomposition by various technical efforts inversely highlights the strength of the pCMD approach, which is simple and hardly depends on various technical conditions.

4.3. Dependence on WISE Color

Another main purpose of this paper is to understand the relationship between stellar population complexity and recent star formation activity in a galaxy. While the

stellar population complexity is measured by the pCMD color dispersion, we use photometric information in the infrared bands to estimate the star formation activities of the target galaxies.

Jarett et al. (2017) showed how the infrared color-color ([3.4] – [4.6] versus [4.6] – [12]) diagram classifies galaxies according to their star formation and AGN activities. Based on the scheme, Figure 15 shows that the morphological types of our sample galaxies are strongly correlated with their star formation activities. While all of our sample galaxies are in the non-AGN domain ([3.4] – [4.6] < 0.8), the spiral galaxies are clearly redder (more active star formation) than the elliptical galaxies in the [4.6] – [12] color, except for two bulge-dominated spiral galaxies. Edge-on disk galaxies are in the intermediate domain between elliptical and spiral galaxies, although several elliptical galaxies and two bulge-dominated spiral galaxies also share that domain. Note that the edge-on disk galaxies in our sample tend to be bulge-dominated rather than disk-dominated, and thus they may be intrinsically similar to bulge-dominated spiral galaxies.

In Figure 16, we compare the pCMD parameters and the total infrared colors of the sample galaxies. There is a strong correlation between [4.6] – [12] and $\min(g-r)_{\mu_r \leq 23.2}$, whereas $\max(g-r)_{\mu_r \leq 23.2}$ shows no clear correlation with [4.6] – [12]. The former trend is as expected, because blue optical color and red infrared color are commonly the signals of star formation activity. Since star-forming spiral galaxies often have red bulges, the latter trend is also understood. However, when we consider the elliptical galaxies only, no significant correlation is found between [4.6] – [12] and $\min(g-r)_{\mu_r \leq 23.2}$. That is, the elliptical galaxies with small excess in infrared color show no difference in $\min(g-r)_{\mu_r \leq 23.2}$ from the elliptical galaxies without infrared-color excess. On the other hand, for the elliptical galaxies, $\min(\sigma(g-r))_{\mu_r \leq 21.2}$ and $\max(\sigma(g-r))_{20.0 \leq \mu_r \leq 21.0}$ appear to be correlated with [4.6] – [12]: the elliptical galaxies with larger [4.6] – [12] tend to have larger $\min(\sigma(g-r))_{\mu_r \leq 21.2}$ and $\max(\sigma(g-r))_{20.0 \leq \mu_r \leq 21.0}$, as shown in Panels (c) and (d) of Figure 16.

The Pearson correlation coefficients and their p-values between several pCMD parameters and the WISE color are listed in Table 1. This table quantitatively shows that $\min(g-r)_{\mu_r \leq 23.2}$, $\min(\sigma(g-r))_{\mu_r \leq 21.2}$ and $\max(\sigma(g-r))_{20.0 \leq \mu_r \leq 21.0}$ are significantly correlated or anti-correlated with [4.6] – [12], whereas $\max(g-r)_{\mu_r \leq 23.2}$ shows no significant correlation, for the whole sample. On the other hand, such trends are somewhat different when only elliptical galaxies are considered:

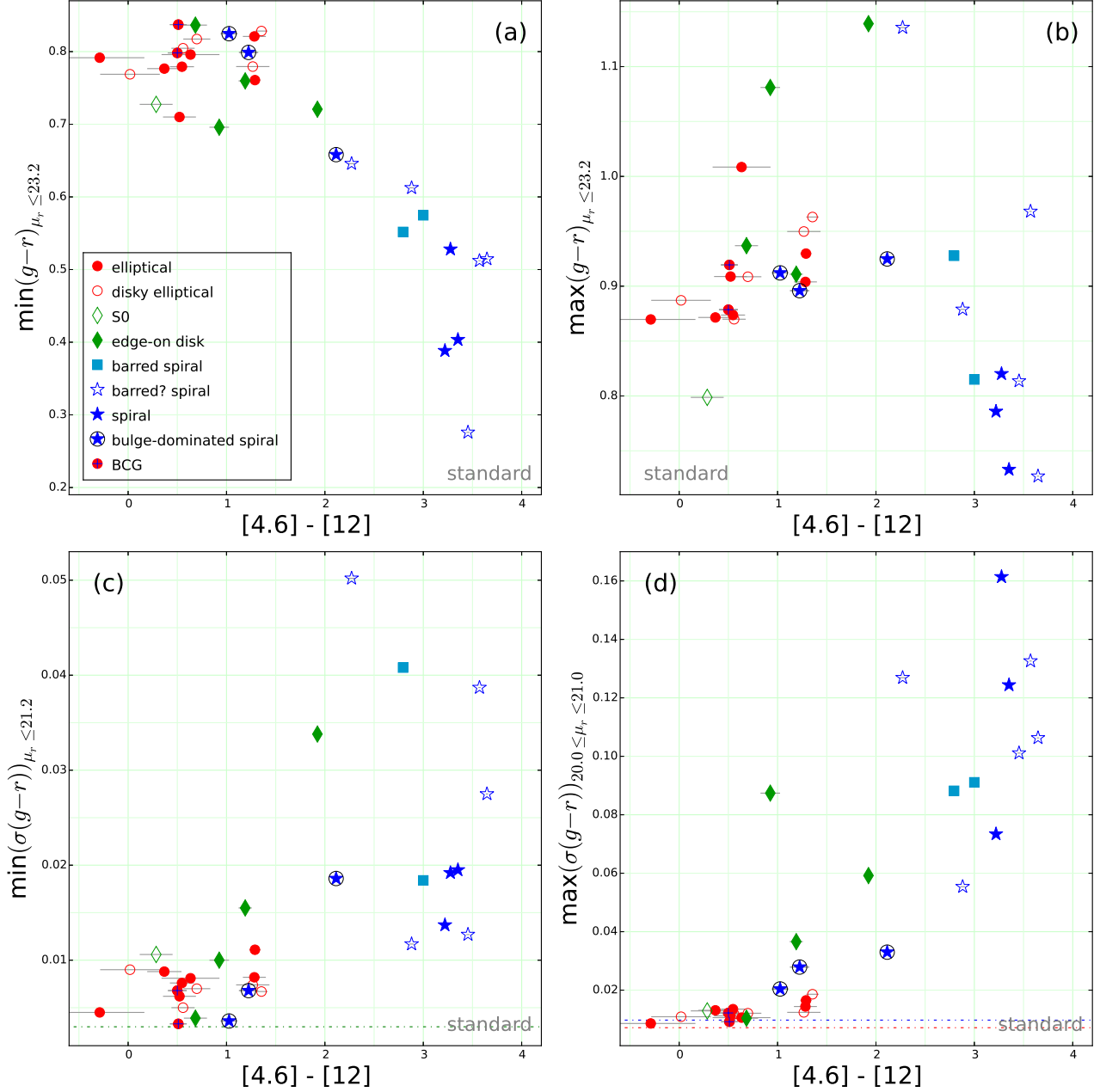


FIG. 16.— The pCMD parameters versus the WISE $[4.6] - [12]$ color, based on the pCMDs after the standard masking procedure: (a) the minimum $g - r$ color at $\mu_r \leq 23.2$ mag arcsec $^{-2}$, (b) the maximum $g - r$ color at $\mu_r \leq 23.2$ mag arcsec $^{-2}$, (c) the minimum $g - r$ color dispersion at $\mu_r \leq 21.2$ mag arcsec $^{-2}$, and (d) the maximum $g - r$ color dispersion at $20.0 \leq \mu_r \leq 21.0$ mag arcsec $^{-2}$. The dot-dashed lines are the reliability limits as described in Figure 10.

$\min(\sigma(g - r))_{\mu_r \leq 21.2}$ shows a marginal correlation and $\max(\sigma(g - r))_{20.0 \leq \mu_r \leq 21.0}$ shows a more significant correlation. It is also noted that $\max(g - r)_{\mu_r \leq 23.2}$ has a marginal correlation with $[4.6] - [12]$ when elliptical and disk elliptical galaxies are considered together, while it has an anti-correlation when spiral galaxies are considered only. All of these trends do not significantly change even when we use the results from the alternative procedure (Appendix B).

Table 4 lists the pCMD parameter values of the sample galaxies from the standard procedure and their WISE colors, which are used in Figures 10 - 16. The WISE colors used in Appendix B are the same as those in Table 4.

5. DISCUSSION

5.1. Issues on Masking

There are some fundamental difficulties in masking contaminants. In the case of early-type galaxies or edge-on disk galaxies, the masking is relatively easy: the SE-detection-based masking works well, because they hardly have confusing internal substructures. After the SE-detection-based masking, possibly remaining contaminants will be covered by the pCMD outlier masking, although it may sometimes over-mask internal substructures such as tidal debris.

What does matter is the late-type galaxies. Basically,

TABLE 4
PCMD PARAMETERS FROM THE STANDARD PROCEDURE, AND WISE COLORS

| Name | $\min(g-r)$ $\mu_r \leq 23.2$ | $\max(g-r)$ $\mu_r \leq 23.2$ | $\mu_r(\text{tip})$ | $\min(\sigma(g-r))$ $\mu_r \leq 21.2$ | $\max(\sigma(g-r))$ $20.0 \leq \mu_r \leq 21.0$ | $\max(\sigma(g-r))$ $18.5 \leq \mu_r \leq 19.5$ | $\max(\sigma(g-r))$ $\mu_r \leq 21.2$ | [3.4] – [4.6] | [4.6] – [12] |
|--------------|----------------------------------|----------------------------------|---------------------|--|--|--|--|--------------------|--------------------|
| A1139-00001 | 0.798 | 0.879 | 17.44 | 0.007 | 0.012 | 0.013 | 0.013 | -0.025 ± 0.012 | 0.500 ± 0.096 |
| A1139-00002 | 0.727 | 0.799 | 16.80 | 0.011 | 0.013 | 0.013 | 0.017 | -0.017 ± 0.009 | 0.285 ± 0.167 |
| A1139-00003 | 0.710 | 0.909 | 17.98 | 0.006 | 0.011 | 0.012 | 0.016 | -0.052 ± 0.012 | 0.522 ± 0.167 |
| A1139-00004 | 0.552 | 0.928 | 18.29 | 0.041 | 0.088 | 0.071 | 0.103 | 0.080 ± 0.012 | 2.794 ± 0.026 |
| A1139-00005 | 0.805 | 0.870 | 17.35 | 0.005 | 0.012 | 0.012 | 0.012 | -0.031 ± 0.010 | 0.558 ± 0.118 |
| A1139-00006 | 0.613 | 0.879 | 17.77 | 0.012 | 0.055 | 0.037 | 0.055 | 0.057 ± 0.010 | 2.881 ± 0.022 |
| A1139-00007 | 0.761 | 0.930 | 17.24 | 0.011 | 0.017 | 0.048 | 0.049 | 0.002 ± 0.009 | 1.289 ± 0.057 |
| A1139-00008 | 0.799 | 0.896 | 17.78 | 0.007 | 0.028 | 0.017 | 0.028 | 0.008 ± 0.010 | 1.224 ± 0.097 |
| A1139-00009 | 0.658 | 0.925 | 17.81 | 0.019 | 0.033 | 0.049 | 0.049 | 0.114 ± 0.011 | 2.114 ± 0.032 |
| A1139-00010 | 0.777 | 0.872 | 17.03 | 0.009 | 0.013 | 0.014 | 0.014 | -0.033 ± 0.011 | 0.368 ± 0.174 |
| A1139-00011 | 0.721 | 1.139 | 18.41 | 0.034 | 0.059 | 0.136 | 0.136 | 0.024 ± 0.010 | 1.924 ± 0.041 |
| A1139-00012 | 0.779 | 0.874 | 17.18 | 0.008 | 0.013 | 0.015 | 0.015 | -0.018 ± 0.013 | 0.547 ± 0.122 |
| A1139-00013 | 0.760 | 0.911 | 17.71 | 0.015 | 0.037 | 0.052 | 0.052 | -0.011 ± 0.010 | 1.190 ± 0.067 |
| A1139-00014 | 0.769 | 0.887 | 17.32 | 0.009 | 0.011 | 0.017 | 0.017 | -0.009 ± 0.011 | 0.019 ± 0.303 |
| A1139-00015 | 0.388 | 0.786 | 19.14 | 0.014 | 0.073 | 0.016 | 0.074 | 0.053 ± 0.016 | 3.220 ± 0.021 |
| A1139-00016 | 0.575 | 0.815 | 17.51 | 0.018 | 0.091 | 0.033 | 0.091 | 0.111 ± 0.014 | 3.000 ± 0.024 |
| A1139-00017 | 0.512 | 0.968 | 18.54 | 0.039 | 0.133 | 0.116 | 0.136 | 0.159 ± 0.009 | 3.571 ± 0.011 |
| A2589-00001 | 0.837 | 0.919 | 17.52 | 0.003 | 0.009 | 0.005 | 0.016 | -0.068 ± 0.011 | 0.510 ± 0.085 |
| A2589-00002 | 0.696 | 1.081 | 16.93 | 0.010 | 0.087 | 0.070 | 0.087 | -0.014 ± 0.012 | 0.926 ± 0.100 |
| A2589-00003 | 0.514 | 0.727 | 17.16 | 0.028 | 0.106 | 0.055 | 0.123 | 0.237 ± 0.010 | 3.647 ± 0.011 |
| A2589-00004 | 0.276 | 0.814 | 17.35 | 0.013 | 0.101 | 0.032 | 0.101 | 0.117 ± 0.012 | 3.454 ± 0.016 |
| A2589-00005 | 0.404 | 0.733 | 18.20 | 0.019 | 0.124 | 0.044 | 0.124 | 0.117 ± 0.017 | 3.352 ± 0.023 |
| A2589-00006 | 0.792 | 0.870 | 17.39 | 0.004 | 0.009 | 0.009 | 0.009 | -0.049 ± 0.014 | -0.289 ± 0.454 |
| A2589-00007 | 0.825 | 0.912 | 17.54 | 0.004 | 0.020 | 0.010 | 0.020 | 0.001 ± 0.012 | 1.026 ± 0.085 |
| A2589-00008 | 0.828 | 0.963 | 17.51 | 0.007 | 0.019 | 0.048 | 0.048 | -0.007 ± 0.013 | 1.355 ± 0.063 |
| A2589-00010 | 0.821 | 0.904 | 17.71 | 0.008 | 0.014 | 0.032 | 0.032 | -0.036 ± 0.021 | 1.283 ± 0.117 |
| A2589-00011 | 0.528 | 0.820 | 18.82 | 0.019 | 0.161 | 0.029 | 0.161 | 0.087 ± 0.014 | 3.276 ± 0.024 |
| A2589-00012 | 0.817 | 0.909 | 17.58 | 0.007 | 0.012 | 0.010 | 0.015 | -0.014 ± 0.012 | 0.698 ± 0.137 |
| A2589-00013 | 0.837 | 0.937 | 17.02 | 0.004 | 0.010 | 0.006 | 0.011 | -0.049 ± 0.012 | 0.684 ± 0.117 |
| A2589-00014* | 0.779 | 0.950 | 17.66 | 0.007 | 0.012 | 0.023 | 0.023 | -0.048 ± 0.045 | 1.267 ± 0.169 |
| A2589-00015 | 0.646 | 1.136 | 18.46 | 0.050 | 0.127 | 0.157 | 0.157 | 0.168 ± 0.011 | 2.271 ± 0.033 |
| A2589-00018 | 0.796 | 1.008 | 17.75 | 0.008 | 0.011 | 0.022 | 0.023 | -0.019 ± 0.015 | 0.634 ± 0.294 |

NOTE. — * The WISE colors of A2589-00014 is based on the profile-fit magnitudes, whereas those of all the other targets are based on the elliptical aperture magnitudes. See Section 2.3 for details.

it is very difficult to perfectly mask contaminants in and around a face-on late-type galaxy with complex spiral arms, because their substructures and contaminants are often too similar to be distinguished. Thus, in the standard procedure, we omitted the SE-detection-based masking for such targets, but only conducted the pCMD outlier masking that works alone to some extent. However, this means that different masking processes are applied to early- and late-type galaxies, which may cause unfair comparison of the pCMD features between galaxies with different morphological types.

The alternative masking procedure was devised to complement such weakness of the standard procedure. Through the alternative procedure, fair comparison is possible between galaxies with any morphological types. However, the $R(\mu_r)$ -based masking is less efficient than the SE-detection-based masking for early-type galaxies. It may fail to mask faint contaminants or contaminants very close to the target galaxy center. Moreover, the $R(\mu_r)$ -based masking may not cover the faint outskirts of a contaminating object due to the limit of the masking algorithm. Thus, it is recommendable to rely on the standard masking procedure if the sample consists of only early-type and edge-on galaxies. The main purpose of the alternative masking procedure is to check how reliable the results from the standard procedure are, by comparing them with the results from a self-consistent masking procedure.

Section 4.2.2 and Appendix B show that the results from the standard procedure and from the alternative procedure are not significantly different from each other. This is because our analysis in this paper focuses on the major trend in the pCMD of each galaxy rather than its fine features. The consistency between the results from the different procedures, despite the weakness of each masking procedure, indicates that the major trend of a pCMD is hardly influenced by the details of the masking methods.

5.2. Morphological Segregation

We tested various combinations of parameters measured from the pCMDs of our sample galaxies, to examine how galaxies with different morphological types are quantitatively distinguished in their pCMD features. As a result, we found that the best parameter set to classify galaxy morphology based on pCMDs is the combination of the minimum color dispersion at $\mu_r \leq 21.2$ mag arcsec⁻² and the maximum color dispersion at $20.0 \leq \mu_r \leq 21.0$ mag arcsec⁻², assisted by axis ratio (Figure 13).

Although these parameters were empirically selected, the underlying mechanism in which they work is relatively easy to understand. As revealed in the pCMDs and the μ_r contour maps, $\max(\sigma(g-r))_{20.0 \leq \mu_r \leq 21.0}$ represents how complex the stellar populations are at the regions where the disk component begins to be dominant in a typical late-type galaxy. In other words, $\max(\sigma(g-r))_{20.0 \leq \mu_r \leq 21.0}$ is dominated by the bulge stellar populations for an early-type galaxy, whereas it is largely affected by the disk stellar populations for a late-type galaxy. That makes $\max(\sigma(g-r))_{20.0 \leq \mu_r \leq 21.0}$ a good indicator of disk dominance, because disks tend to have complex stellar populations spatially not uniform whereas bulges and elliptical galaxies have relatively uni-

form stellar populations.

Figure 17 shows twelve examples of radial profiles with structural decomposition using the GALFIT, which partially supports this interpretation (but not perfectly). For galaxies with $B/T > 0.6$, the stellar populations at $20.0 \leq \mu_r \leq 21.0$ mag arcsec⁻² are dominated by bulge components. On the other hand, for galaxies with $B/T < 0.5$, the stellar populations at $20.0 \leq \mu_r \leq 21.0$ mag arcsec⁻² are affected more significantly by disk components.

Nevertheless, the bulge-disk decomposition does not perfectly explain the performance of $\max(\sigma(g-r))_{20.0 \leq \mu_r \leq 21.0}$, because there are some exceptional cases. For example, some bulge-dominated spiral galaxies (A1139-00009 and A2589-00007) have large B/T ratios and their stellar populations at $20.0 \leq \mu_r \leq 21.0$ mag arcsec⁻² seem to be dominated by their bulge components. Despite the fact that their B/T ratios are even larger than that of the S0 galaxy A1139-00002 (0.65 and 0.91 versus 0.61), their $\max(\sigma(g-r))_{20.0 \leq \mu_r \leq 21.0}$ values are larger than that of the S0 galaxy (0.036 and 0.020 versus 0.015). On the other hand, a disk elliptical galaxy A2589-00012 has a relatively small B/T (0.40), but its $\max(\sigma(g-r))_{20.0 \leq \mu_r \leq 21.0}$ is as small as 0.015. This indicates that the bulge-disk decomposition is not the only reason that $\max(\sigma(g-r))_{20.0 \leq \mu_r \leq 21.0}$ works. A spiral galaxy, even though it is extremely bulge-dominated (e.g., A2589-00007), seems to have more complex stellar populations compared to an early-type galaxy with a similar B/T ratio. That is, the pCMD color dispersion is a good indicator to detect such fine difference in stellar populations that is hardly caught in classical methods of structural decomposition.

Note that $\mu_r = 21.2$ mag arcsec⁻² is the analysis limit for color dispersion in our data and thus the performance of color dispersion at $\mu_r > 21.2$ mag arcsec⁻² cannot be probed in this paper. If deeper images with sufficient S/N even at $\mu_r > 21.2$ mag arcsec⁻² are used, the usefulness of color dispersion as an indicator of galaxy morphology may be even larger, because the photometric properties of fainter part in a disk will be reflected. For example, in Figure 17, the disk component of A1139-00002 (S0) is small, but it becomes relatively dominant at $R > 10''$ (total $\mu_r \gtrsim 22.2$ mag arcsec⁻²). Thus, it may be useful even in distinguishing between elliptical and S0 galaxies if the color dispersion at lower surface brightness is available.

On the other hand, $\min(\sigma(g-r))_{\mu_r \leq 21.2}$ represents the minimum complexity of stellar populations, typically (but not necessarily) at the brightest center. Although elliptical galaxies and bulges of late-type galaxies typically have simple structures, they may show unusual substructures sometimes, which result in large color dispersion at their pCMD tips (e.g., A1139-00007 and A2589-00008). Since such substructures are thought to originate from mergers or interactions, $\min(\sigma(g-r))_{\mu_r \leq 21.2}$ can be used as a simple indicator of recent mass assembly events of a target galaxy: larger $\min(\sigma(g-r))_{\mu_r \leq 21.2}$ for more complex history of recent mass assembly on average. This may not be a very precise indicator but will be useful particularly in a statistical study, because it can be conveniently applied to a bulk of galaxies, if appropriate corrections are conducted for the difference in

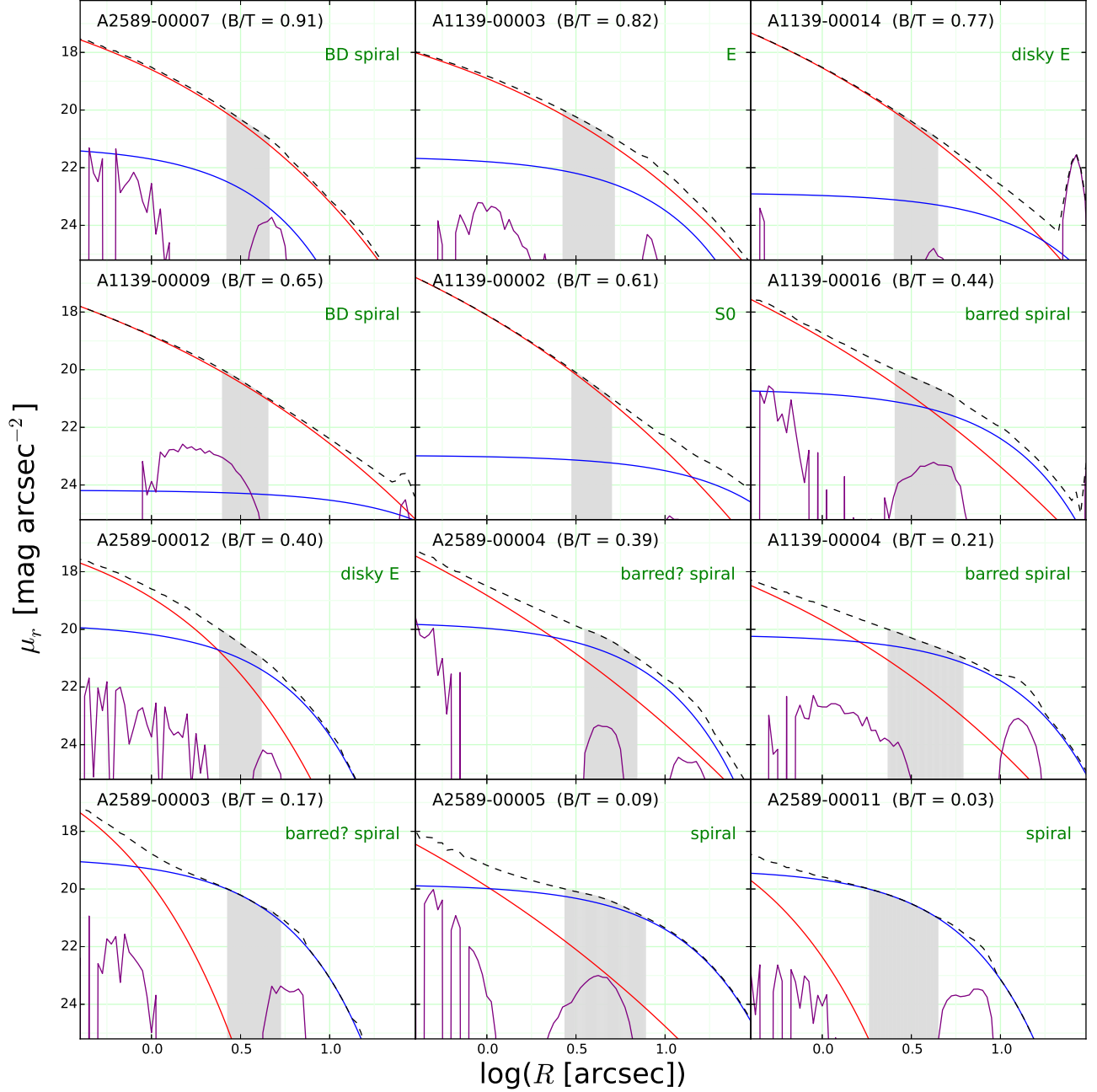


FIG. 17.— Radial profiles with structural decomposition using the GALFIT, for twelve galaxies having various B/T ratios (0.03 – 0.91). Each galaxy is decomposed using a Sersic component (bulge; red line) and an exponential profile (disk; blue line). The purple line shows the residual light and the black dashed line is the total (bulge + disk + residual) profile in each panel. The radial regime corresponding to the total surface brightness between 20.0 – 21.0 mag arcsec⁻² is shaded on each plot.

redshift and spatial resolution.

It is interesting that the best parameter to characterize galaxy morphology is color dispersion rather than color index itself. In other words, for morphological classification of galaxies, it is more effective to compare how well mixed the stellar populations are rather than to see how old or metal-rich on average they are. The latter also works to some extent, but it fails to discriminate bulge-dominated spiral galaxies from elliptical galaxies in our results. This is not strange because the correlation between galaxy morphology and galaxy color is known to be not very tight (e.g., blue early-type galaxies and red late-type galaxies; Lee et al. 2006, 2008; Tojeiro et al.

2013).

However, for the generalized application of the morphological classification using the pCMD features, additional work is required. First of all, a much larger number of galaxies with well-classified morphological types need to be tested to get more reliable criteria of morphological classification. Our sample size of 32 is absolutely insufficient to establish criteria that can be generally applied. Furthermore, it is necessary to examine how the criteria of morphological classification change as a function of image resolution. Since the pCMD features strongly depend on image resolution (Lee et al. 2011, 2012; Conroy & van Dokkum 2016), its effect on the pCMD classifica-

tion should be seriously considered, to apply this method to galaxies at various redshifts. Nevertheless, if these issues are addressed, the pCMD classification method will be a valuable technique to automatically classify a huge number of galaxies in the future imaging surveys using next generation facilities such as the Large Synoptic Survey Telescope (LSST; Ivezić et al. 2008).

5.3. Recent Growth of Elliptical Galaxies

In Section 4.3, the elliptical galaxies show a marginal correlation between their $\min(\sigma(g-r))_{\mu_r \leq 21.2}$ and $[4.6] - [12]$ (Figure 16(c)) and a stronger correlation between $\max(\sigma(g-r))_{20.0 \leq \mu_r \leq 21.0}$ and $[4.6] - [12]$ (Figure 16(d)). Since the color dispersion reflects how complex stellar populations are in a galaxy, this result indicates that the elliptical galaxies with more complex stellar populations tend to have recently experienced more active star formation (or vice versa). According to some previous studies, the recent growth of massive elliptical galaxies mainly depend on dry mergers rather than gas-rich mergers (Naab et al. 2006; Kormendy et al. 2009; Bernardi et al. 2011). On the other hand, some other studies found the evidence of recent star formation activities probably triggered by mergers in some massive elliptical galaxies (Kaviraj et al. 2009; Fernández-Ontiveros et al. 2011; Sheen et al. 2016). Our result supports the latter findings: the recent star formation activity and mass growth of massive elliptical galaxies appear to be correlated with each other in our sample. Thus, the recent growth of those elliptical galaxies may not entirely depend on dry mergers, but gas-rich minor mergers may have usually happened.

One may suspect that the complexity of stellar populations in those galaxies may not necessarily originate from merger events, but it may be naturally caused by recent star formation not from merger origins. Even in that case, however, the recent star formation must have been spatially not uniform at scales larger than 600 pc ($\sim 0.8''$ in our images) to enlarge the color dispersion in a pCMD. It may require anisotropic infall of gas. Gas interactions without disturbance of stellar orbits can be such an origin, which may happen even for cluster galaxies with high encounter velocities (Park & Hwang 2009). Although the exact origin of the recent star formation cannot be determined in this paper, it is plausible that some environmental effects acted on the large color dispersion in a pCMD.

The interpretation of the $\max(g-r)_{\mu_r \leq 23.2}$ versus $[4.6] - [12]$ plot (Figure 16(b)) is somewhat complicated (Figure 16(b)). At first glance, the data points seem to be randomly scattered in this plot. However, as shown in Table 1, we find two opposite trends when we inspect the sub-samples of the elliptical + disky elliptical galaxies and the spiral galaxies: (1) the elliptical galaxies with infrared-color excess tend to have redder maximum pCMD color, but (2) on the other hand, the spiral galaxies are getting bluer in the optical band as infrared color increases.

These two opposite trends imply that multiple physical origins may be involved in the $\max(g-r)_{\mu_r \leq 23.2}$ versus $[4.6] - [12]$ relation. For example, the marginal correlation of elliptical + disky elliptical galaxies may result from dust remnants in some elliptical galaxies. That is, elliptical galaxies that have recently experienced star formation may have remaining dust, which cause red in-

frared color (due to remaining warm dust) and red optical color (by dust extinction) at the same time. On the other hand, spiral galaxies with redder infrared color may have more active current star formation unlike elliptical galaxies, and thus they tend to have blue optical color due to a large amount of young stars that cannot be sufficiently obscured by dust. It will be worth checking if these trends are established still in a sufficiently large sample of galaxies in future studies.

6. CONCLUSION

We analyzed the pixel color-magnitude diagrams (pCMDs) of 32 bright galaxies in two galaxy clusters A1139 and A2589 at low redshifts. We yielded the pCMDs of the sample galaxies using the SE-detection-based masking or the $R(\mu_r)$ -based masking, any of which is complemented by the subsequent pCMD outlier masking process. We compared the results from the two procedures with each other, and confirmed that the different masking methods do not significantly affect the major trends of pCMD properties.

Our main conclusions from the pCMD analysis of the target galaxies are as follows:

1. At least in our sample, the early- and late-type galaxies are most clearly separated by the combination of the minimum color dispersion at $\mu_r \leq 21.2$ mag arcsec⁻² and the maximum color dispersion at $20.0 \leq \mu_r \leq 21.0$ mag arcsec⁻², while the edge-on galaxies are discriminated by using axis ratio. This is because $\min(\sigma(g-r))_{\mu_r \leq 21.2}$ represents the minimum complexity of stellar populations typically at the brightest center, whereas $\max(\sigma(g-r))_{20.0 \leq \mu_r \leq 21.0}$ reflects the complexity of stellar populations at the disk component in a typical spiral galaxy.
2. The color dispersion measurements ($\min(\sigma(g-r))_{\mu_r \leq 21.2}$ and $\max(\sigma(g-r))_{20.0 \leq \mu_r \leq 21.0}$) of an elliptical galaxy appear to be correlated with its total infrared color ($[4.6] - [12]$). This indicates that the complexity of stellar populations in an elliptical galaxy is closely related with its recent star formation activity. From this observational evidence, we infer that gas-rich minor mergers or gas interactions may have usually happened during the recent growth of massive elliptical galaxies.

In both conclusions, the color dispersion in a pCMD is a key quantity that appears to be closely related with the structure and formation history of a galaxy. Unlike the various pCMD features that are more complicated such as the backbone curvature and the spatial distribution of outlying pixels (Lee et al. 2017), the color dispersion can be simply measured and applied to a bulk of galaxies, to trace their recent formation histories. However, the definition and usage of this parameter need to be improved and more variously examined, because it must depend on rest-frame wavelength and spatial resolution of target images. Our follow-up studies using the full sample of the KYDISC clusters will cover this topic.

We appreciate the anonymous referee who gave us comments very helpful to improve this paper. In this

work, we used the data obtained under the K-GMT Science Program funded through Korea GMT Project operated by Korea Astronomy and Space Science Institute

(KASI). Parts of this research were conducted by the Australian Research Council Centre of Excellence for All Sky Astrophysics in 3 Dimensions (ASTRO 3D), through project number CE170100013.

REFERENCES

- Abraham, R. G., Ellis, R. S., Fabian, A. C., Tanvir, N. R., & Glazebrook, K. 1999, *MNRAS*, 303, 641
- Assaf, R. J., Kochanek, C. S., Brodwin, M., et al. 2010, *ApJ*, 713, 970
- Bernardi, M., Roche, N., Shankar, F., & Sheth, R. K. 2011, *MNRAS*, 412, L6
- Bertin, E., & Arnouts, S. 1996, *A&AS*, 117, 393
- Bothun, G. D. 1986, *AJ*, 91, 507
- Conroy, C., & van Dokkum, P. G. 2016, *ApJ*, 827, 9
- de Grijs, R., Lee, J. T., Mora Herrera, M. C., Fritze-v. Alvensleben, U., & Anders, P. 2003, *New Astron.*, 8, 155
- Dressler, A. 1987, *ApJ*, 317, 1
- Fernández-Ontiveros, J. A., López-Sanjuan, C., Montes, M., Prieto, M. A., & Acosta-Pulido, J. A. 2011, *MNRAS*, 411, L21
- Fisher, D. B., & Drory, N. 2008, *AJ*, 136, 773
- Gadotti, D. A. 2009, *MNRAS*, 393, 1531
- George, K. 2017, *A&A*, 598, 45
- Ivezic, Z., Axelrod, T., Brandt, W. N., et al. 2008, *Serbian Astronomical Journal*, 176, 1
- Jarrett, T. H., Cluver, M. E., Magoulas, C., et al. 2017, *ApJ*, 836, 182
- Jarrett, T. H., Cohen, M., Masci, F., et al. 2011, *ApJ*, 735, 112
- Kaviraj, S., Peirani, S., Khochfar, S., Silk, J., & Kay, S. 2009, *MNRAS*, 394, 1713
- Kim, K., Oh, S., Jeong, H., et al. 2016, *ApJS*, 225, 6
- Ko, J., Chung, H., Hwang, H. S., & Lee, J. C. 2016, *ApJ*, 820, 132
- Kormendy, J., Fisher, D. B., Cornell, M. E., & Bender, R. 2009, *ApJS*, 182, 216
- Lanyon-Foster, M. M., Conselice, C. J., & Merrifield, M. R. 2007, *MNRAS*, 380, 571
- Larson, R. B. 1974, *MNRAS*, 166, 585
- Lee, J., & Yi, S. K. 2013, *ApJ*, 766, 38
- Lee, J. H., Lee, M. G., & Hwang, H. S. 2006, *ApJ*, 650, 148
- Lee, J. H., Kim, S. C., Park, H. S., Ree, C. H., Kyeong, J., & Chung, J. 2011, *ApJ*, 740, 42
- Lee, J. H., Kim, S. C., Ree, C. H., et al. 2012, *ApJ*, 754, 80
- Lee, J. H., Kim, M., Ree, C. H., et al. 2013, *ApJ*, 762, L4
- Lee, J. H., Lee, M. G., Park, C., & Choi, Y.-Y. 2008, *MNRAS*, 389, 1791
- Lee, J. H., Oh, S., Jeong, H., Yi, S. K., Kyeong, J., & Park, B.-G. 2017, *ApJ*, 844, 81
- Liu, F. S., Jiang, D., Gui, Y., et al. 2016, *ApJ*, 822, L25
- Naab, T., Khochfar, S., & Burkert, A. 2006, *ApJ*, 636, L81
- Oh, S., Kim, K., Lee, J. H., et al. 2017, *ApJS*, submitted
- Oser, L., Ostriker, J. P., Naab, T., Johansson, P. H., & Burkert, A. 2010, *ApJ*, 725, 2312
- Park, C., & Hwang, H. 2009, *ApJ*, 699, 1595
- Pastrello, N., Forbes, D. A., Usher, C., et al. 2015, *MNRAS*, 451, 2625
- Patridge, R. R., & Peebles, P. J. E. 1967, *ApJ*, 147, 868
- Peng, C. Y., Ho, L. C., Impey, C. D. & Rix, H.-W. 2002, *AJ*, 124, 266
- Peng, C. Y., Ho, L. C., Impey, C. D. & Rix, H.-W. 2002, *AJ*, 139, 2097
- Schlafly, E. F., & Finkbeiner, D. P. 2011, *ApJ*, 737, 103
- Searle, L., & Zinn, R. 1978, *ApJ*, 225, 357
- Sheen, Y.-K., Smith, R., Jaffé, Y., et al. 2017, *ApJ*, 840, L7
- Sheen, Y.-K., Yi, S. K., Ree, C. H., Jaffé, Y., Demarco, R., & Treister, E. 2016, *ApJ*, 827, 32
- Skrutskie, M. F., Cutri, R. M., Stiening, R., et al. 2006, *AJ*, 131, 1163
- Tinsley, B. M. 1972, *ApJ*, 178, 319
- Tojeiro, R., Masters, K. L., Richards, J., et al. 2013, *MNRAS*, 432, 359
- Toomre, A. 1977, in *The Evolution of Galaxies and Galaxy Populations*, ed. B. M. Tinsley & R. B. Larsen (New Haven: Yale Univ. Obs.), 401
- van Dokkum, P. G., Whitaker, K. E., Brammer, G., et al. 2010, *ApJ*, 709, 1018
- Wright, E. L., Eisenhardt, P. R. M., Mainzer, A. K., et al. 2010, *AJ*, 140, 1868
- York, D. G., Adelman, J. Anderson, J. E., Jr., et al. 2000, *AJ*, 120, 1579

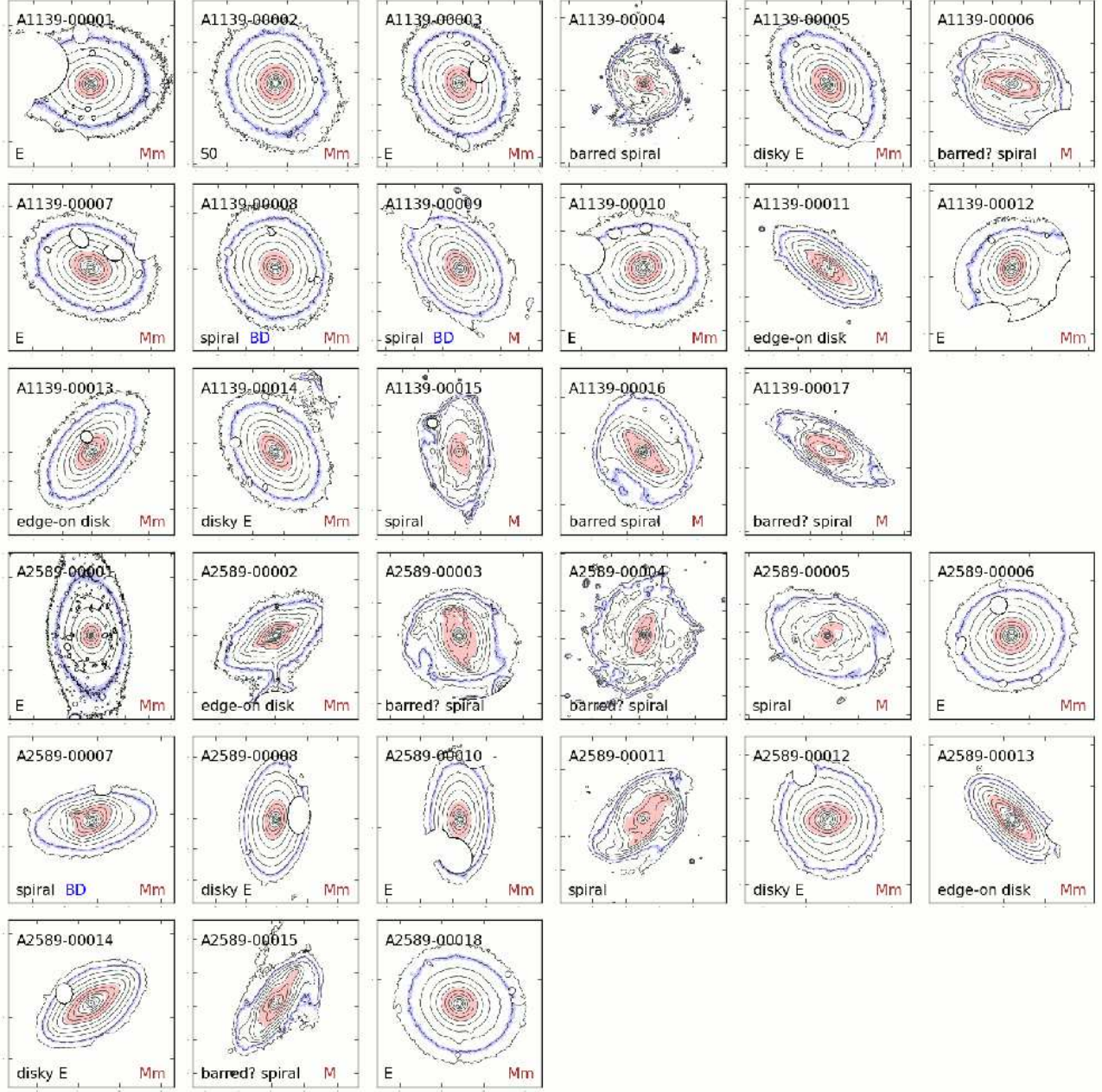


FIG. 18.— Surface brightness contour maps after the SE-detection-based masking. The letters at the lower right corner indicates the sort of masking: ‘M’ indicates that the target galaxy was masked using the SE detection with large background meshes only, while ‘Mm’ indicates that the target galaxy was masked using the SE detection with small background meshes (m) as well as the SE detection with large background meshes (M). The regions colored with faint red show the pixels with $20.0 \leq \mu_r \leq 21.0$ mag arcsec $^{-2}$, while the regions colored with faint blue denote the pixels on the analysis limit ($\mu_r = 23.2$ mag arcsec $^{-2}$).

APPENDIX

A. FULL PLOTS IN THE MASKING PROCESSES

In Figure 6, we schematically summarized the masking processes in the standard and alternative procedures. However, the full plots showing the detailed masking processes for the whole sample galaxies were omitted to improve the readability of this paper. In this section, those full plots are presented.

The masking processes in the standard procedure flow as shown in Figures 18 – 20:

1. The target galaxies are masked using the SE detection (Figure 18). The SE-detection-based masking is adaptively applied with consideration of the morphology of a target galaxy and the performance of the masks. Among the 32 sample galaxies, 20 galaxies are masked using the SE detection with both of large and small background

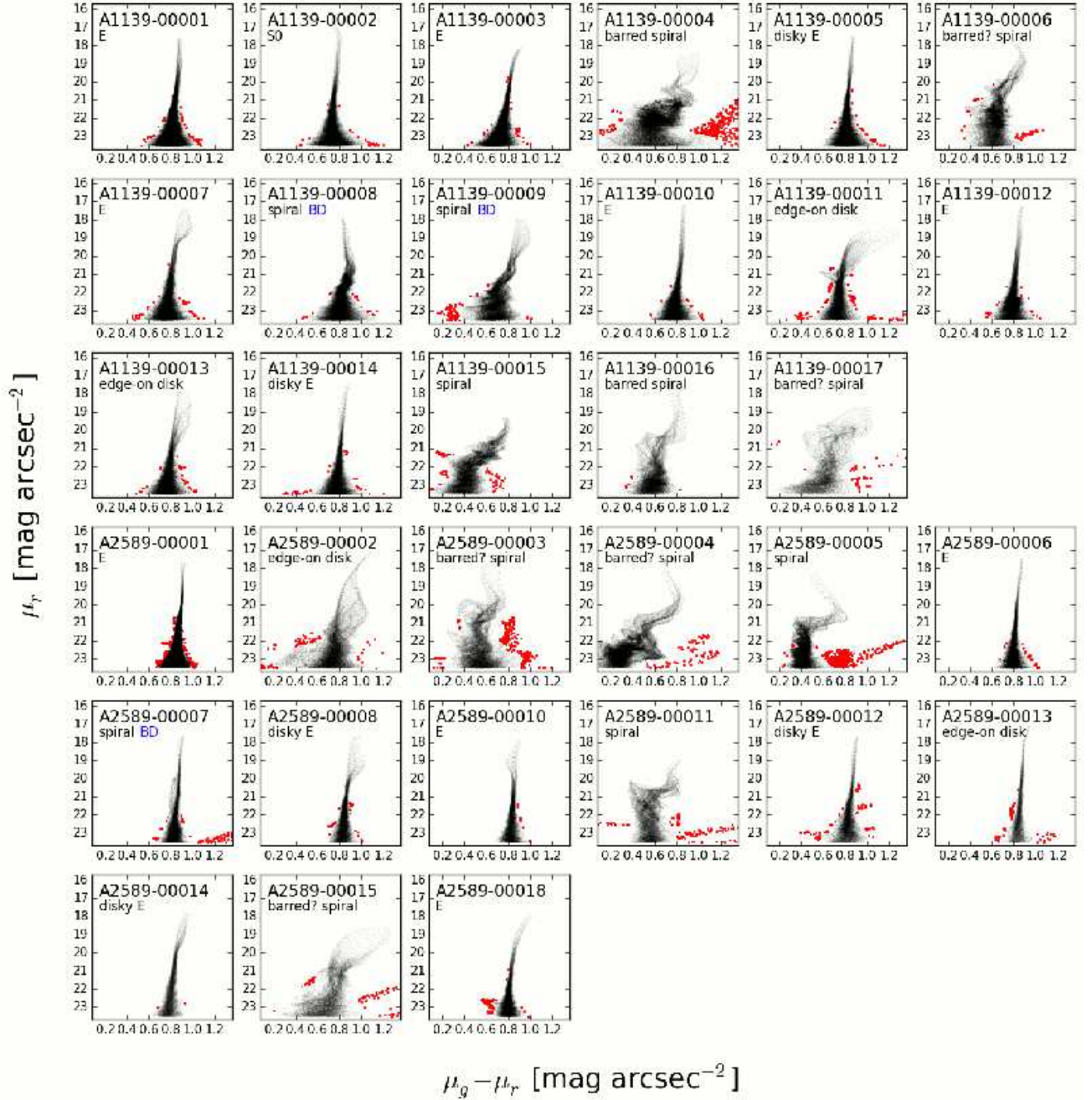


FIG. 19.— The pCMDs after the SE-detection-based masking and the smoothing with the $0.8''$ -aperture spline kernel. Red dots show the pCMD outliers (see Section 3.1 for details).

- meshes ('Mm'), whereas eight galaxies are masked using the SE detection only with large background meshes ('M'). The rest four galaxies are not masked at all.
- Using the pCMDs after the SE-detection-based masking, outlying pixels are determined with the method described in Section 3.1 (Figure 19). Some of the selected outliers may be substructures of target galaxies, but the possible over-masking does not significantly change the major trends of pCMDs.
 - The pCMD outliers and their neighboring pixels within $0.8''$ distance (seeing size) are additionally masked, because those neighboring pixels may also be affected by the contaminants (Figure 20). This additional masking is particularly important for late-type galaxies, which are poorly masked in the SE-detection-based method.

The final pCMDs after these processes are shown in Figure 7.

The full plots for the alternative procedure are also presented in Figures 21 – 23, and the final pCMDs are shown in Figure 8. Although the pCMDs resulting from the first-step masking in the two procedures is pretty different from

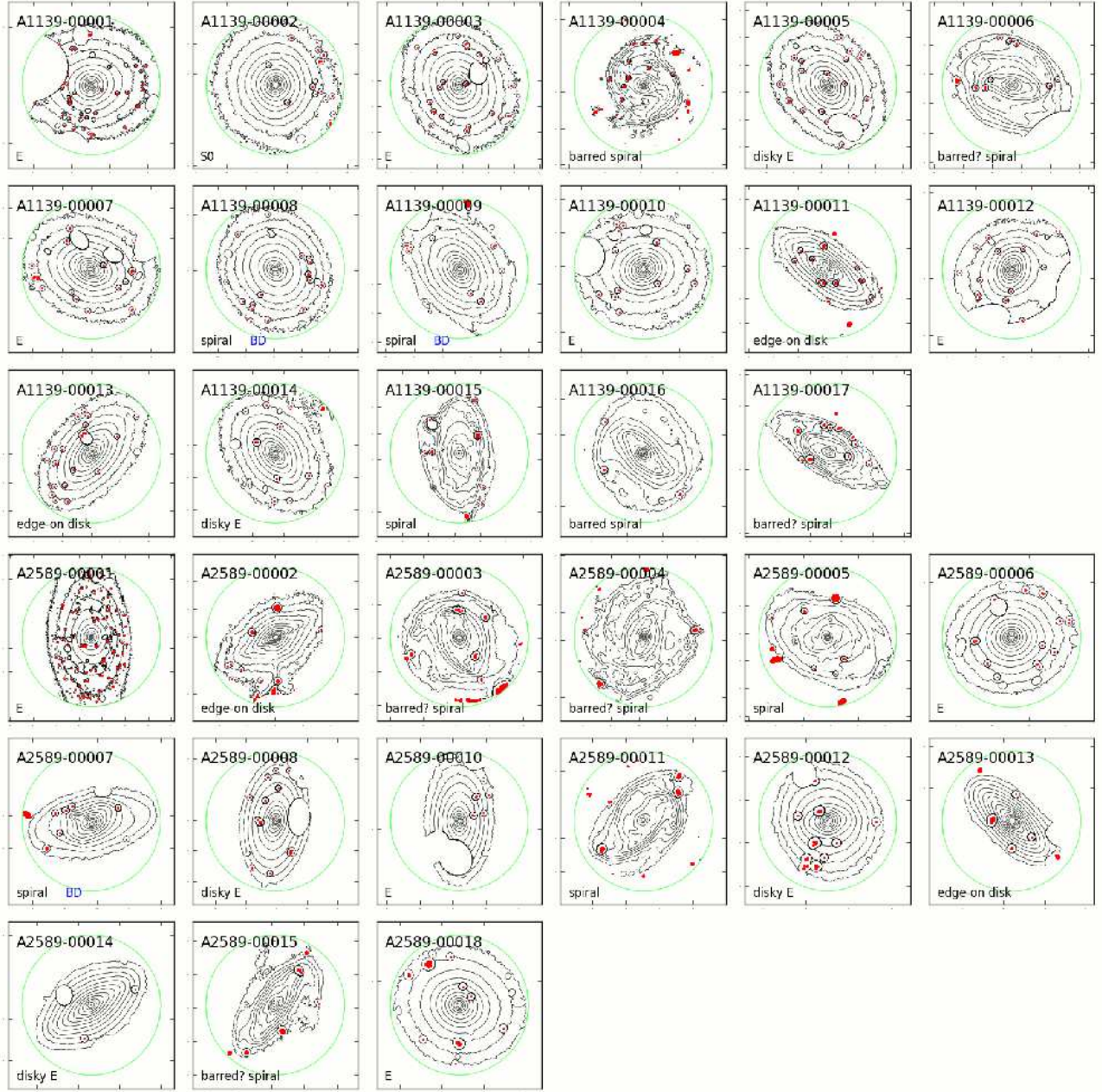


FIG. 20.— Surface brightness contour maps after masking pCMD outliers and their neighboring pixels within $0.8''$. The outlying pixels defined in Figure 19 are marked as red dots. The green circle indicates the spatial extent for the final pixel analysis of each target, which is defined at Step 2 of the alternative procedure in Section 3.2.

each other (Figures 19 and 22), the difference of the final pCMDs is smaller (Figures 7 – 9), owing to the secondary masking process based on pCMD outliers.

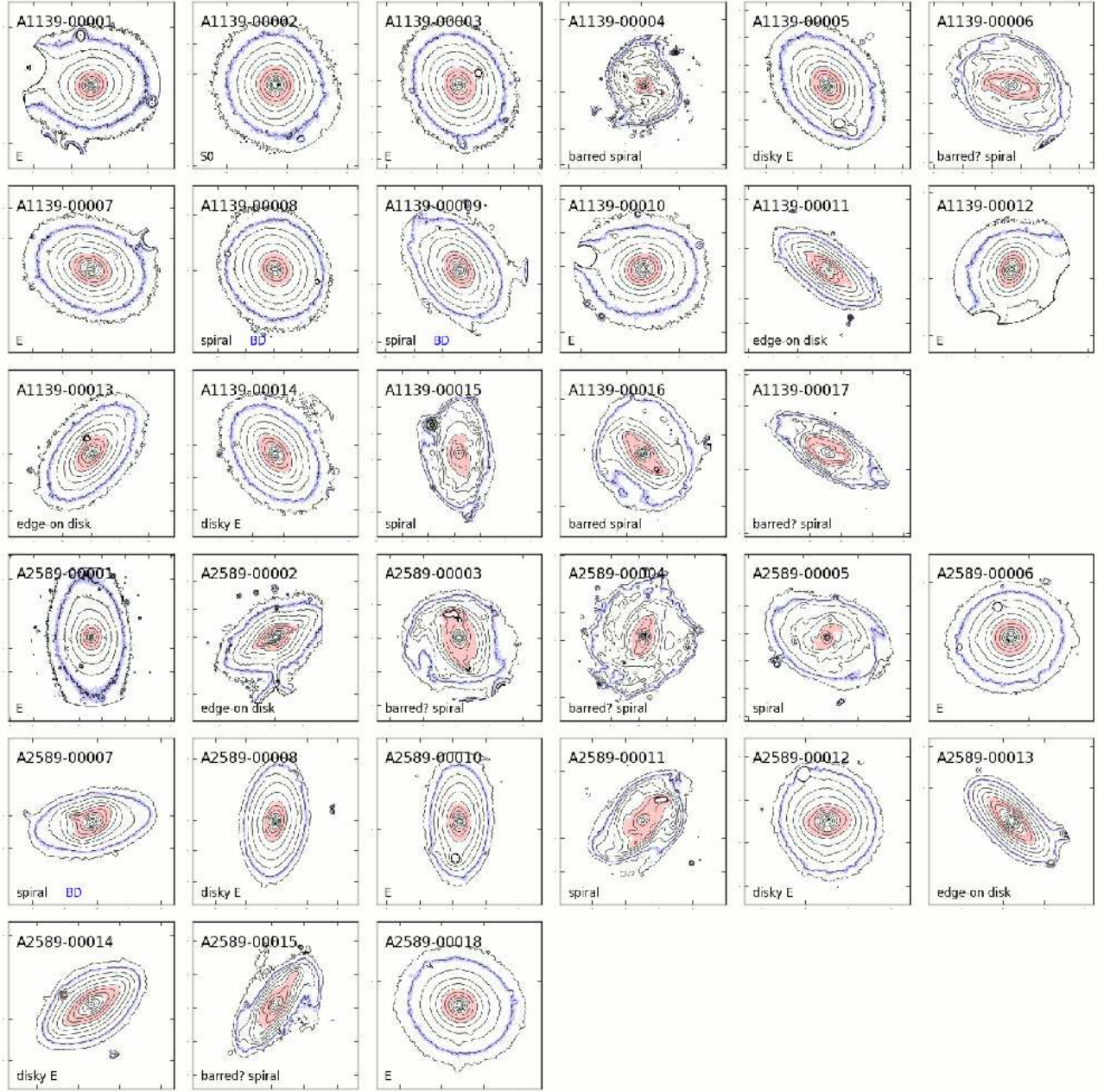


FIG. 21.— Surface brightness contour maps after the $R(\mu_r)$ -based masking: the same as Figure 18, except that these are from the alternative masking procedure.

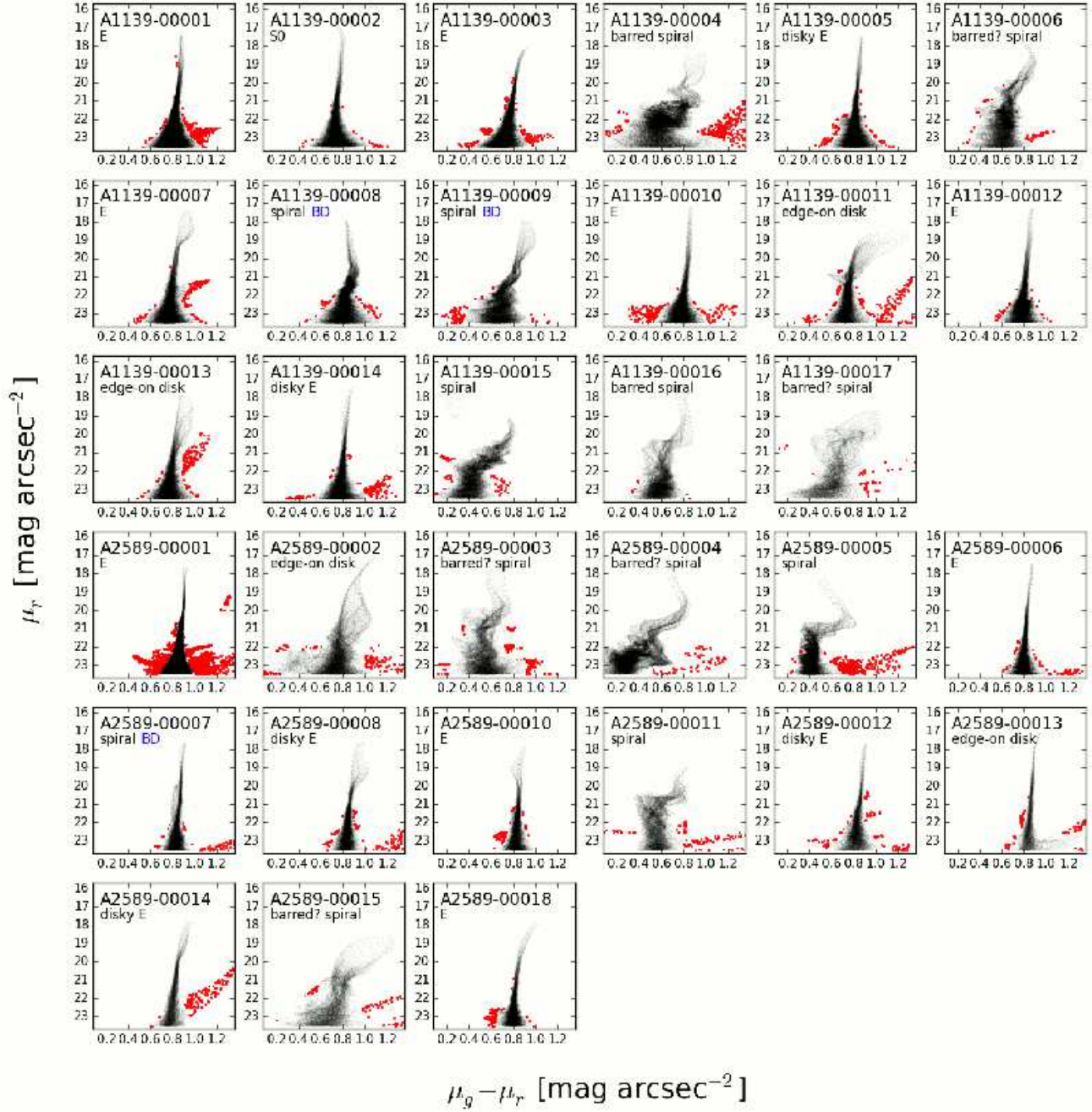


FIG. 22.— The pCMDs after the $R(\mu_r)$ -based masking and the smoothing with the $0.8''$ -aperture spline kernel: the same as Figure 19, except that these are from the alternative masking procedure.

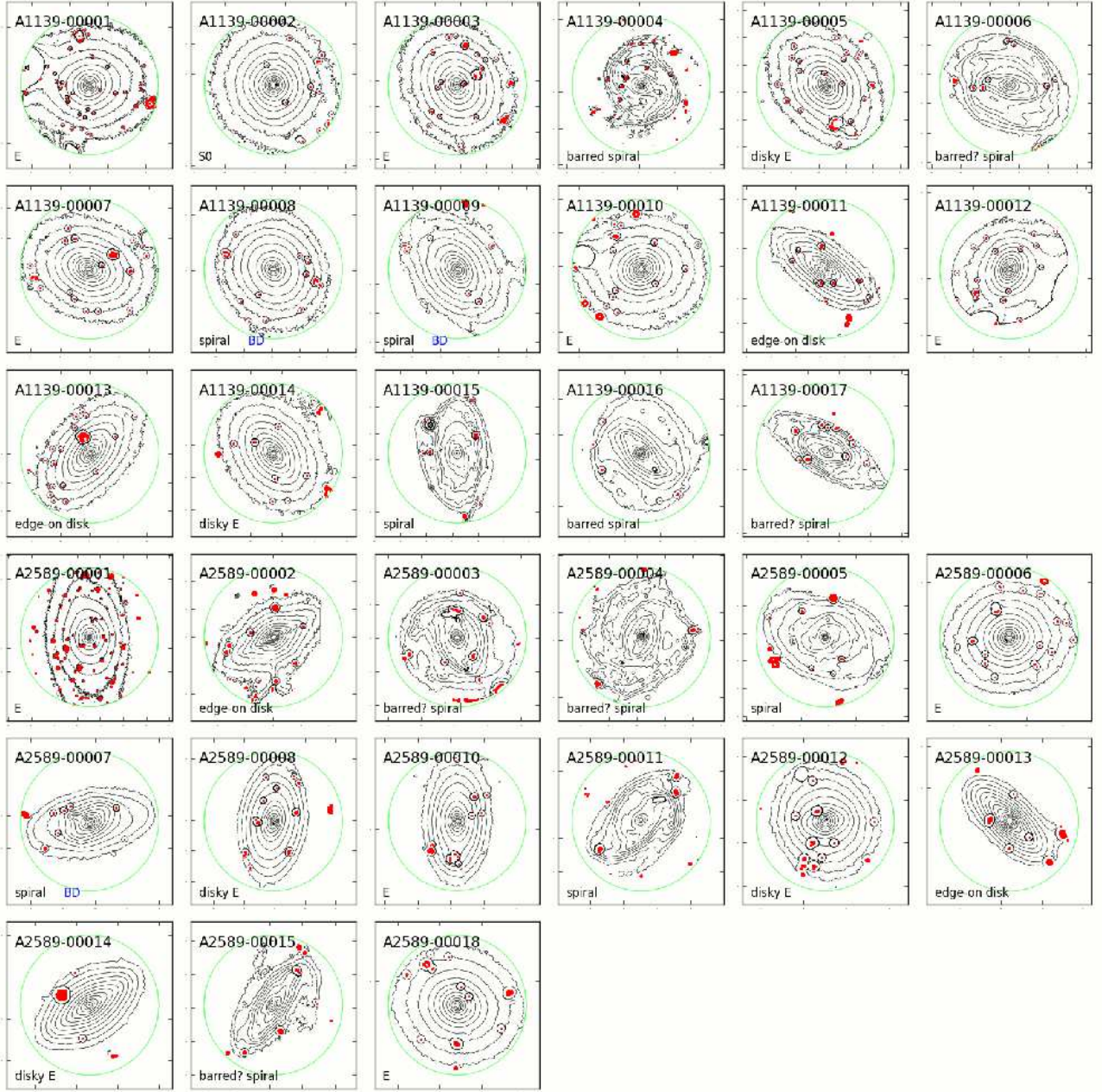


FIG. 23.— Surface brightness contour maps after masking pCMD outliers and their neighboring pixels within $0.8''$: the same as Figure 20, except that these are from the alternative masking procedure.

TABLE 5
PCMD PARAMETERS FROM THE ALTERNATIVE PROCEDURE

| Name | $\min(g-r)$ $\mu_r \leq 23.2$ | $\max(g-r)$ $\mu_r \leq 23.2$ | $\mu_r(\text{tip})$ | $\min(\sigma(g-r))$ $\mu_r \leq 21.2$ | $\max(\sigma(g-r))$ $20.0 \leq \mu_r \leq 21.0$ | $\max(\sigma(g-r))$ $18.5 \leq \mu_r \leq 19.5$ | $\max(\sigma(g-r))$ $\mu_r \leq 21.2$ |
|-------------|----------------------------------|----------------------------------|---------------------|--|--|--|--|
| A1139-00001 | 0.797 | 0.879 | 17.18 | 0.007 | 0.012 | 0.014 | 0.014 |
| A1139-00002 | 0.727 | 0.799 | 16.80 | 0.011 | 0.013 | 0.013 | 0.017 |
| A1139-00003 | 0.708 | 0.909 | 17.98 | 0.006 | 0.011 | 0.012 | 0.016 |
| A1139-00004 | 0.552 | 0.928 | 18.29 | 0.041 | 0.089 | 0.071 | 0.103 |
| A1139-00005 | 0.799 | 0.870 | 17.35 | 0.005 | 0.012 | 0.012 | 0.012 |
| A1139-00006 | 0.600 | 0.879 | 17.77 | 0.012 | 0.055 | 0.037 | 0.055 |
| A1139-00007 | 0.760 | 0.930 | 17.24 | 0.011 | 0.017 | 0.048 | 0.049 |
| A1139-00008 | 0.800 | 0.896 | 17.78 | 0.007 | 0.028 | 0.017 | 0.028 |
| A1139-00009 | 0.655 | 0.925 | 17.81 | 0.019 | 0.033 | 0.049 | 0.049 |
| A1139-00010 | 0.772 | 0.872 | 17.03 | 0.009 | 0.013 | 0.014 | 0.014 |
| A1139-00011 | 0.721 | 1.139 | 18.41 | 0.034 | 0.059 | 0.136 | 0.136 |
| A1139-00012 | 0.779 | 0.874 | 17.18 | 0.008 | 0.013 | 0.015 | 0.015 |
| A1139-00013 | 0.759 | 0.911 | 17.71 | 0.015 | 0.037 | 0.052 | 0.052 |
| A1139-00014 | 0.769 | 0.887 | 17.32 | 0.009 | 0.011 | 0.017 | 0.017 |
| A1139-00015 | 0.237 | 0.786 | 16.81 | 0.013 | 0.074 | 0.245 | 0.245 |
| A1139-00016 | 0.575 | 0.815 | 17.51 | 0.018 | 0.089 | 0.033 | 0.089 |
| A1139-00017 | 0.512 | 0.968 | 18.54 | 0.039 | 0.133 | 0.116 | 0.136 |
| A2589-00001 | 0.837 | 0.919 | 17.52 | 0.003 | 0.009 | 0.005 | 0.016 |
| A2589-00002 | 0.696 | 1.081 | 16.93 | 0.010 | 0.087 | 0.070 | 0.087 |
| A2589-00003 | 0.514 | 0.727 | 17.16 | 0.028 | 0.096 | 0.055 | 0.096 |
| A2589-00004 | 0.276 | 0.814 | 17.35 | 0.013 | 0.101 | 0.032 | 0.101 |
| A2589-00005 | 0.404 | 0.733 | 18.20 | 0.019 | 0.124 | 0.044 | 0.124 |
| A2589-00006 | 0.791 | 0.870 | 17.39 | 0.004 | 0.009 | 0.009 | 0.009 |
| A2589-00007 | 0.824 | 0.912 | 17.54 | 0.004 | 0.020 | 0.010 | 0.020 |
| A2589-00008 | 0.830 | 0.963 | 17.51 | 0.007 | 0.019 | 0.048 | 0.048 |
| A2589-00010 | 0.822 | 0.904 | 17.71 | 0.009 | 0.014 | 0.032 | 0.032 |
| A2589-00011 | 0.528 | 0.820 | 18.82 | 0.019 | 0.117 | 0.029 | 0.117 |
| A2589-00012 | 0.818 | 0.908 | 17.58 | 0.007 | 0.012 | 0.010 | 0.015 |
| A2589-00013 | 0.838 | 0.937 | 17.02 | 0.004 | 0.010 | 0.006 | 0.011 |
| A2589-00014 | 0.781 | 0.950 | 17.66 | 0.007 | 0.012 | 0.023 | 0.023 |
| A2589-00015 | 0.646 | 1.136 | 18.46 | 0.050 | 0.127 | 0.157 | 0.157 |
| A2589-00018 | 0.798 | 1.008 | 17.75 | 0.008 | 0.011 | 0.022 | 0.023 |

B. RESULTS FROM THE PCMDS AFTER THE ALTERNATIVE MASKING PROCEDURE

All figures in Section 4 are based on the pCMDs after the standard masking procedure, and the results from the alternative procedure were omitted for better readability. The differences between the final results from the two different procedures are not significant. In this section, those omitted results are presented.

Figures 24, 25, 26 and 27 are the alternative procedure versions of Figures 10, 11, 12 and 16. The results from the alternative procedure show little difference from the results from the standard procedure. Most sample galaxies show little changes in their distributions on the plots, particularly for elliptical galaxies. Only a few spiral galaxies show considerable changes in their pCMD parameters (e.g., A1139-00015 and A2589-00011), which result from incomplete masking of contaminants that happens in spiral galaxies more easily. However, those changes do not affect our main conclusions at all. Table 5 lists the pCMD parameter values of the target galaxies from the alternative procedure, which are used in Figures 24 - 27.

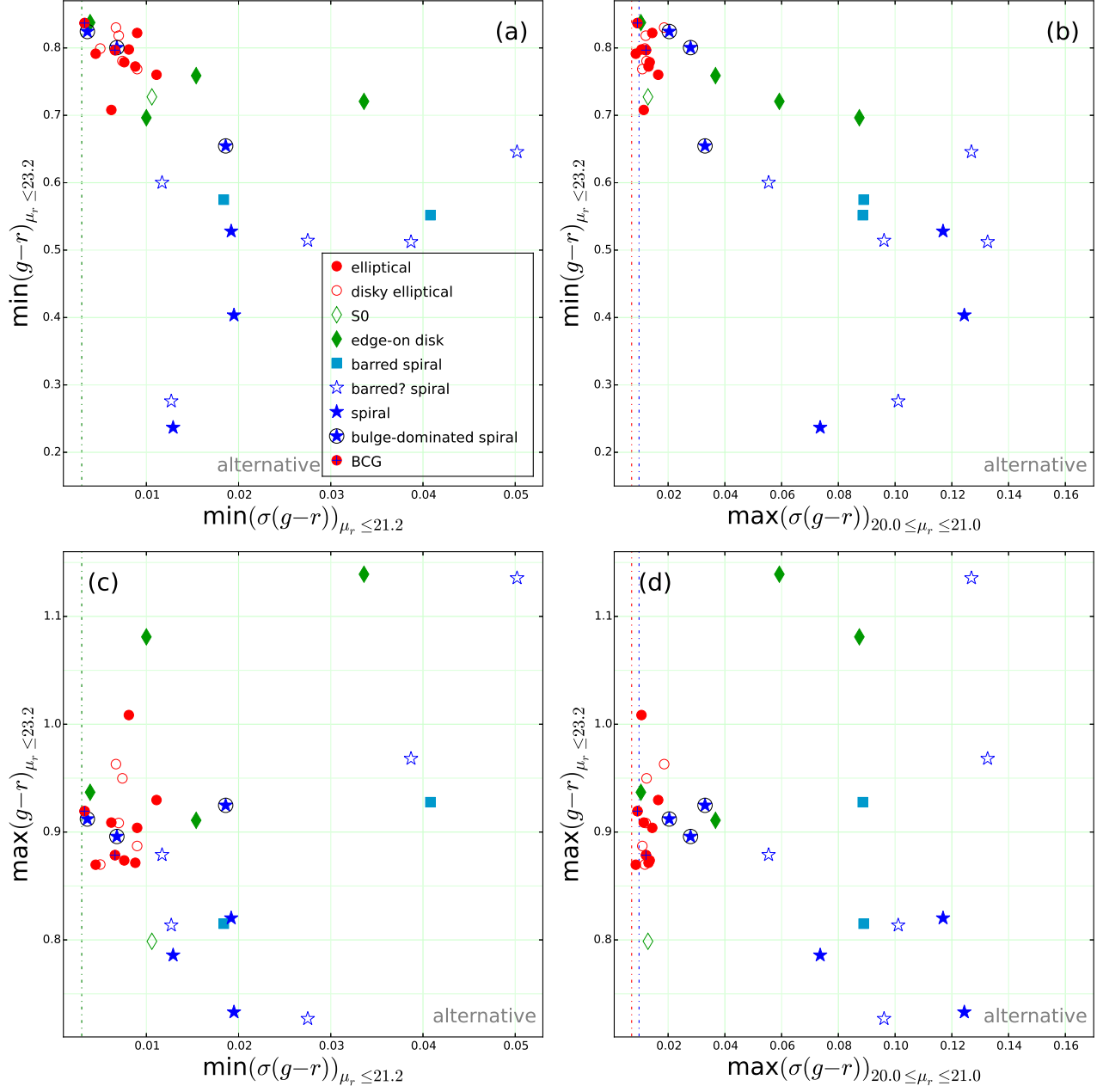


FIG. 24.— Correlations between pCMD parameters, based on the pCMDs after the alternative procedure: (a) the minimum $g-r$ color at $\mu_r \leq 23.2$ mag arcsec $^{-2}$ versus the minimum $g-r$ color dispersion at $\mu_r \leq 21.2$ mag arcsec $^{-2}$, (b) the minimum $g-r$ color at $\mu_r \leq 23.2$ mag arcsec $^{-2}$ versus the maximum $g-r$ color dispersion at $20.0 \leq \mu_r \leq 21.0$ mag arcsec $^{-2}$, (c) the maximum $g-r$ color at $\mu_r \leq 23.2$ mag arcsec $^{-2}$ versus the minimum $g-r$ color dispersion at $\mu_r \leq 21.2$ mag arcsec $^{-2}$, and (d) the maximum $g-r$ color at $\mu_r \leq 23.2$ mag arcsec $^{-2}$ versus the maximum $g-r$ color dispersion at $20.0 \leq \mu_r \leq 21.0$ mag arcsec $^{-2}$. The symbols are the same as those in Figure 10.

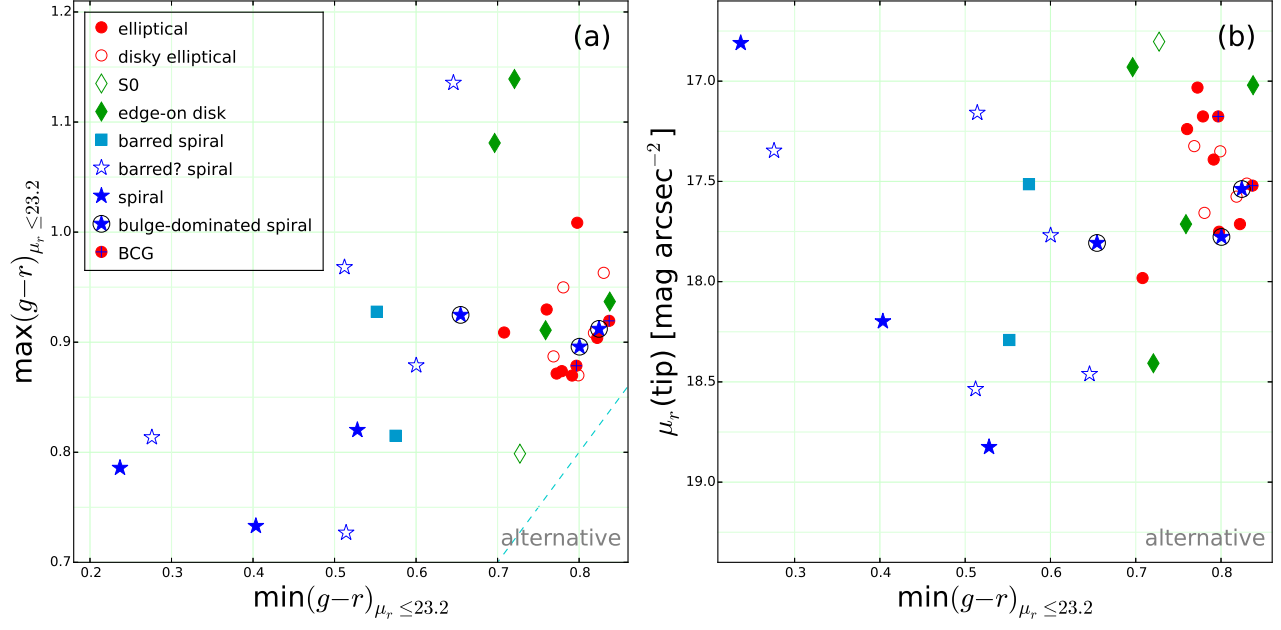


FIG. 25.— (a) The maximum versus minimum values of mean $g-r$ color at $\mu_r \leq 23.2$ mag arcsec $^{-2}$, and (b) the brightest μ_r versus the minimum $g-r$ color at $\mu_r \leq 23.2$ mag arcsec $^{-2}$, based on the pCMDs after the alternative masking procedure. The symbols are the same as those in Figure 11.

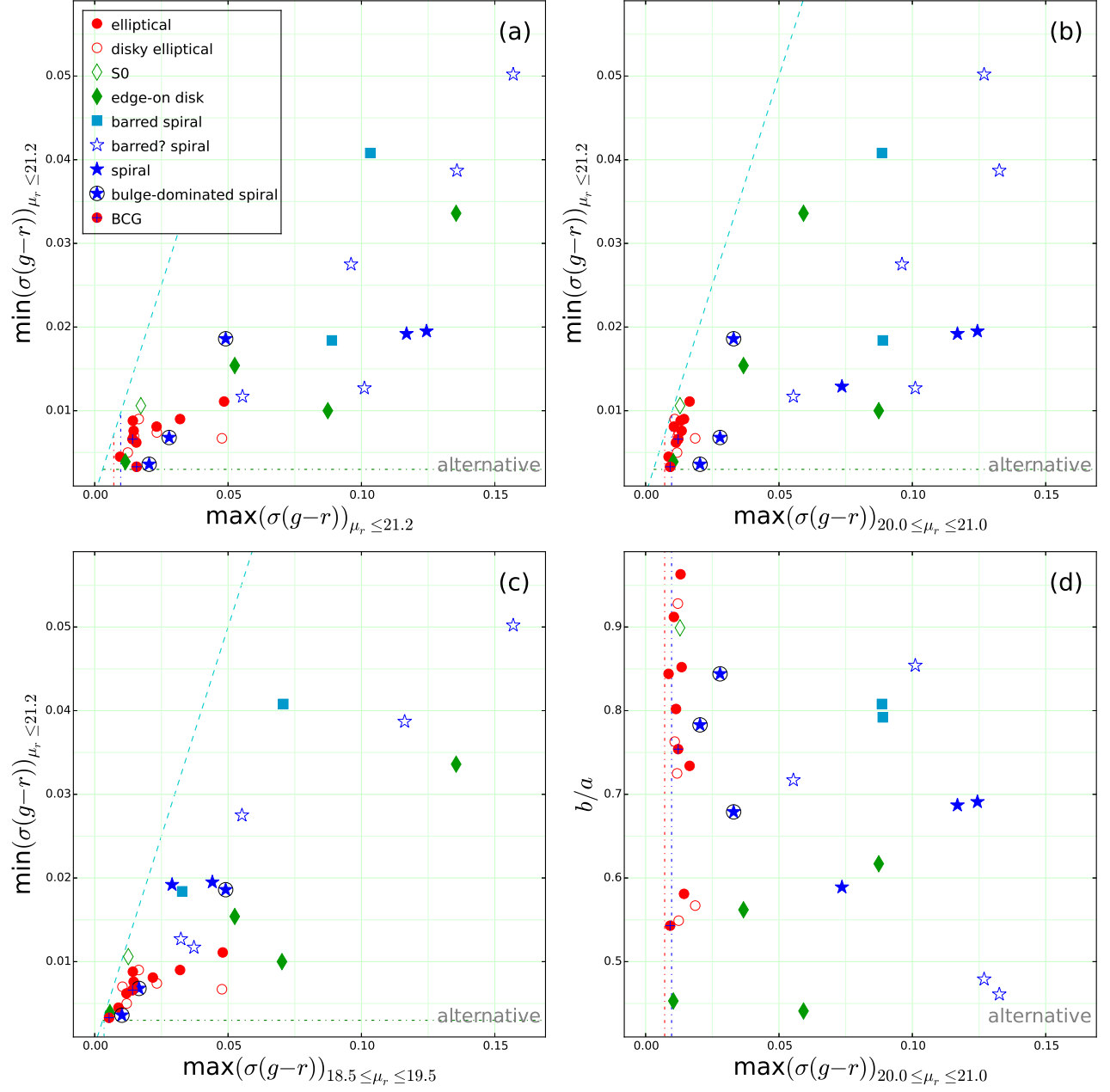


FIG. 26.— The minimum $g-r$ color dispersion at $\mu_r \leq 21.2$ mag arcsec $^{-2}$ (a) versus the maximum $g-r$ color dispersion at $\mu_r \leq 21.2$ mag arcsec $^{-2}$, (b) versus the maximum $g-r$ color dispersion at $20.0 \leq \mu_r \leq 21.0$ mag arcsec $^{-2}$, and (c) versus the maximum $g-r$ color dispersion at $18.5 \leq \mu_r \leq 19.5$ mag arcsec $^{-2}$. (d) Axis ratio versus the maximum $g-r$ color dispersion at $20.0 \leq \mu_r \leq 21.0$ mag arcsec $^{-2}$. These plots are the same as those in Figure 12, except that these are from the alternative masking procedure.

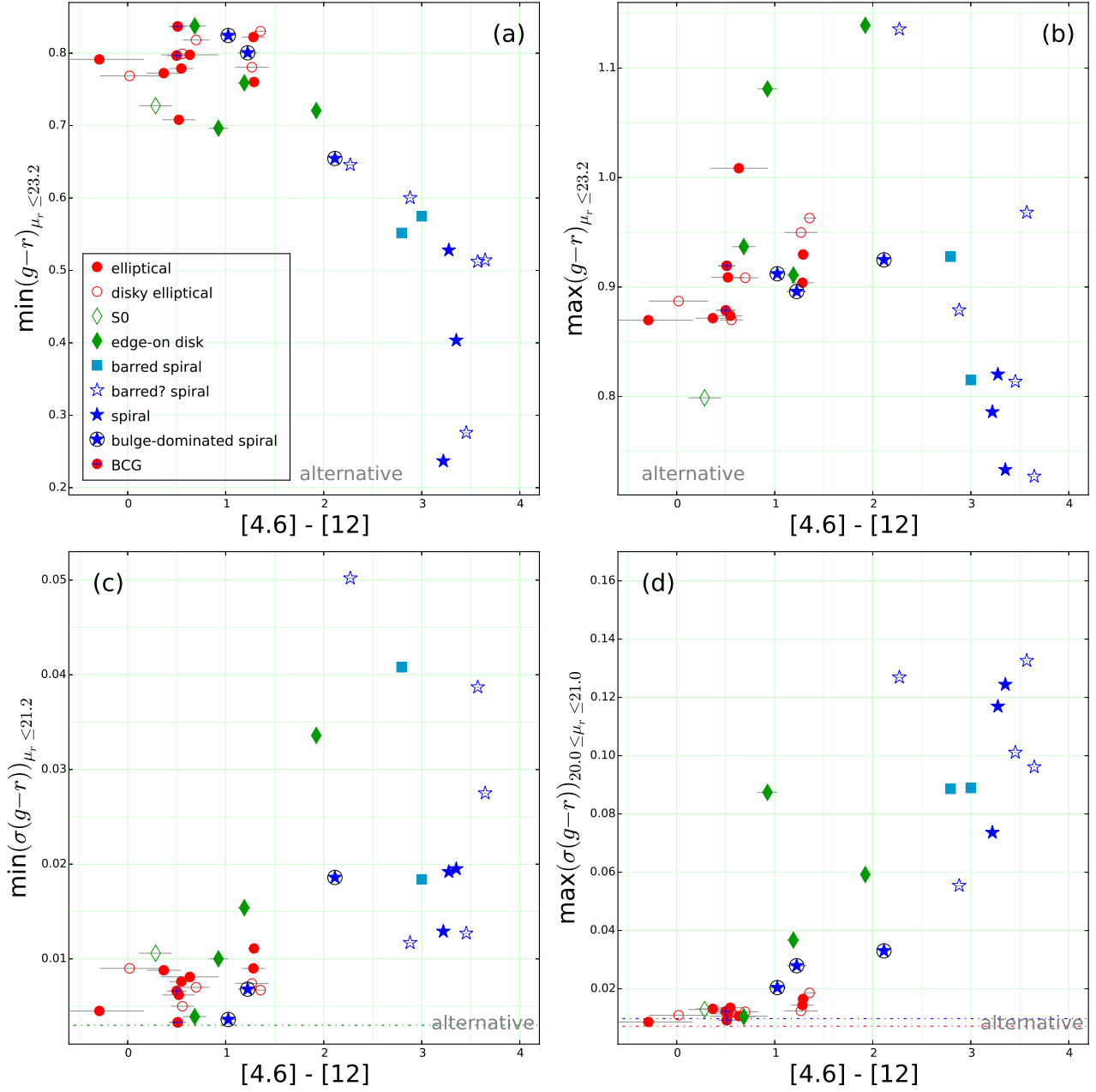


FIG. 27.— The pCMD parameters versus the WISE [4.6] - [12] color, based on the pCMDs after the alternative masking procedure: (a) the minimum $g-r$ color at $\mu_r \leq 23.2$ mag arcsec $^{-2}$, (b) the maximum $g-r$ color at $\mu_r \leq 23.2$ mag arcsec $^{-2}$, (c) the minimum value of $g-r$ color dispersion at $\mu_r \leq 21.2$ mag arcsec $^{-2}$, and (d) the maximum value of $g-r$ color dispersion at $20.0 \leq \mu_r \leq 21.0$ mag arcsec $^{-2}$. The dot-dashed lines are the reliability limits as described in Figure 10.